

Examining meteorological controls on tropical low clouds in satellite observations and climate models

Logan R. Longacre
anx8td@virginia.edu

A thesis submitted to the faculty of the University of Virginia in partial fulfillment of the requirements for the degree of Master's of Science in the department of Environmental Science in the College of Liberal Arts & Sciences

Charlottesville
2024

Abstract.....	3
I. Introduction.....	4
II. Chapter 1: Links between meteorology and tropical boundary layer cloudiness...	11
A. Data & Methods	11
Reanalysis data.....	11
a. NOAA OISST V2	11
b. MERRA-2	12
c. ERA-5.....	12
d. Derived statistics.....	12
Satellite data	14
a. ISCCP.....	14
b. CALIPSO-CASCCAD	14
Regression analysis	16
B. Results.....	17
Relationship of cloudiness and Meteorology.....	17
Connecting cloudiness to temperature through meteorology	19
C. Discussion.....	23
D. Conclusion.....	27
III. Chapter 2: Representation of links between meteorology and tropical boundary layer cloudiness in models.....	28
A. Data and Methods	28
Historical simulations	28
Pre-industrial control simulations.....	29
Regression analysis	30
B. Results.....	31
Relationship of cloudiness and meteorology	31
Connections between temperature and cloudiness mediated by meteorology	34
C. Discussion.....	35
D. Conclusion.....	36
IV. Figures	38
V. References	61

Abstract

Low cloud feedbacks are at the heart of climate model uncertainty of projections of anthropogenic warming. In this work, I aim to quantify the role of local meteorology in controlling stratocumulus (Sc) and shallow trade cumulus (ShCu) cloud fraction throughout the tropics, evaluate regional differences in these relationships, test the robustness of the observed relationships across different datasets, and examine how these relationships are modeled in current state-of-the-art global climate models (GCMs). First, I analyze the covariability of Sc and ShCu with local meteorological cloud controlling factors (CCFs) and assess the responses of Sc, ShCu, and CCFs to interannual surface temperature changes. First, there is generally good agreement among datasets on the sign of the Sc sensitivities to CCFs across the tropics: strong temperature inversions, high free-tropospheric relative humidity (RH_{700}) (with the exception of the northeast Pacific), low sea surface temperatures, strong surface winds, and cold temperature advection all support higher Sc cloudiness. All observational datasets suggest that EIS is the dominant control on Sc cloud fraction. On the other hand, no singular CCF dominantly controls ShCu cloud fraction across the tropics: substantial regional variability is observed in the ShCu-CCF relationships. In general, however, reductions in estimated inversion strength (EIS), relative humidity at 700 hPa (RH_{700}), and subsidence, as well as increases in sea surface temperatures (SST) and warm temperature advection, support a Sc to ShCu transition on the western edges of Sc regions. A complementary analysis is then performed with GCM output to assess model performance in capturing these sensitivities. Compared with observations, tropical Sc and ShCu in GCMs are overly sensitive to EIS, SST, RH_{700} , and vertical velocity and not sensitive enough to wind speed and temperature advection. The largest multi-model mean changes and largest inter-model spread in low cloud fraction (LCF) changes in the tropics occur in the equatorial Pacific in response to EIS, SST, and vertical velocity perturbations. The larger contribution from vertical motion in the models suggests that the modeled low cloud feedback will be more sensitive to future large-scale

overturning (Hadley/Walker) circulation changes than the observations suggest they should be. Finally, the linear model derived from our multiple linear regression analysis of the modeled output does substantially better at predicting LCF changes than the linear model predicting LCF changes in the observations, suggesting that (a) nonlinearities in the real world that are non-trivial to predicting LCF changes are absent from the models and/or (b) the linear model is too limited by the six chosen CCFs. This work emphasizes the importance of using multiple observational datasets to observationally constrain low cloud feedbacks, highlights priorities for improving parameterization of low cloud processes, and underscores the need to expand our analysis of LCF sensitivity to CCFs to include additional predictors and/or nonlinear methods.

I. Introduction

Previous literature has established that the biggest component of uncertainty in global climate model (GCM) projections of future warming for a given emissions scenario remains the impact of changing cloudiness on temperature and climate through changes in radiative fluxes, known as cloud feedback (Ceppi et al. 2017). In general, this response is found to be positive, meaning that changes to clouds and their radiative effects amplify warming due to greenhouse gases; however, GCMs frequently disagree on the magnitude and at times direction of this signal (Ceppi et al. 2017). Changes in tropical cloudiness, in particular, are an outsized contributor to uncertainty in the global cloud feedback (Cesana and Del Genio 2021). Because of the nature of the tropical overturning circulation, with convergence and ascent near the equator and divergence along the descending branch of the Hadley cell, the tropics have distinct regions of high cloudiness and low cloudiness. As the tropical overturning circulation responds to greenhouse gas forcing, changes to the high and low cloud landscapes will also occur (Schiro et al. 2022). Through changing cloud feedback, tropical cloudiness in turn affects the equilibrium climate sensitivity (ECS), which is the forecast change in global mean surface air temperature upon a doubling of atmospheric carbon

dioxide from pre-industrial levels after reaching radiative equilibrium (IPCC 4th Assessment Glossary). As a result, understanding changes in tropical cloudiness is at the heart of improving GCM representation of global warming and enabling a clear representation of the state of the atmosphere. In general, cloud mechanisms have become better understood, such as controls on deep convective height and its effect on longwave radiation, which is a well-known positive feedback referred to as the “cloud altitude” feedback. The mechanisms underpinning other cloud changes, such as cloud amount and optical depth feedbacks, are less well understood.

Under warming, oceanic low cloudiness generally reduces and consequently decreases the planet's average albedo and therefore increases warming (Bony et al. 2015), though the spread in modeled responses is large and highly correlated with climate sensitivity (Cesana and Del Genio 2021; Myers et al. 2021; Schiro et al. 2022; Cesana et al. 2023). In certain parts of the tropics, clouds are a climatological fixture: take, for example, the intertropical convergence zone (ITCZ), where near-equatorial trade winds come together and provide year-round convection, or marine stratocumulus zones like those found off the coasts of Perú or Angola which form in part as a consequence of Coriolis force-related impacts on oceanic currents. Underpinning both of these phenomena are the global circulation. Stratocumulus clouds form in subtropical zones of low sea surface temperatures, persistent subsidence, and a temperature inversion, though details of the exact mechanisms controlling stratocumulus in different ocean basins remain elusive. In the case of the ITCZ, the Hadley cell brings abundant moisture from across the tropics to its ascending branch, leading to extensive tropical cloudiness of all three height domains.

Here, I review what is known about local meteorological controls on tropical low cloudiness. First, sea surface temperatures (SSTs) have been identified as an important thermodynamic driver in the transition from stratocumulus (Sc) cloud to shallow cumulus (ShCu), with increased SSTs corresponding to increased shallow cumulus at the expense of stratocumulus, though there exists

some disagreement on the exact mechanistic pathway behind this signal (Mieslinger et al. 2019). Qu et al. (2015) and Bretherton and Blossey (2014) found further observational and modeled evidence, respectively, that higher sea surface temperatures reduce stratocumulus cloudiness. Scott et al. (2020) lend further credence to this idea, at least for stratocumulus clouds, highlighting both cold temperature advection and cold SSTs as positive drivers of Sc cloudiness.

Humidity is another strong control on the formation of clouds. Without a certain amount of moisture in the air at a given temperature, water vapor cannot condense into the liquid state and form clouds. There are of course an abundance of other microphysical processes regarding condensation which also control cloudiness, but those are wholly irrelevant if the atmosphere is devoid of moisture. That said, these are local processes, which directly impact cloudiness only in their immediate area. Non-local processes regarding humidity are indeed important controls of tropical low cloudiness – for example, consider the humidity not within the boundary layer, but above it, in the free troposphere. Generally, this region is drier than the marine boundary layer (MBL), which leads to entrainment at the interface where the moist MBL air is sapped by the dry free troposphere, a process that can be bolstered by various meteorological processes like vertical motion and enhanced stability, as outlined in Qu et al. (2015) and Bretherton and Blossey (2014). Conversely, if the free troposphere is moist, boundary layer cloudiness should be able to grow upwards without being inhibited by the entrainment of dry air at their interface. This control was confirmed observationally in Myers and Norris (2016), with their findings summarized by Klein et al. (2017) as simply that increased free tropospheric moisture leads to a moister MBL and more cloudiness.

Moreover, the stability of the lower troposphere, though closely related to sea surface temperature and subsidence in certain regions, has a particularly noteworthy relationship with low cloudiness (Klein and Hartmann 1993; Wood and Bretherton 2006; Yue et al. 2011; Myers and

Norris 2013). Stability, especially strong inversions, can both stimulate and repress cloudiness. On one hand, they may prevent upward motion by serving as a strong cap on convection. On the other, they can encourage boundary layer cloudiness by preventing the escape of moisture from the layer and reducing mixing (Wood and Bretherton 2006). Steepening inversions can thus preferentially generate stratocumulus clouds instead of shallow cumulus clouds, and vice versa for weakened inversions. In fact, a sharp boundary has been found, along which cloudiness rapidly transitions from cumuliform to stratiform when the inversion strength reaches 3 K (Myers and Norris 2013).

Scott et al. (2020) found that cold air advection provides an enhancement to upward fluxes of heat and moisture from the surface, which provides an abundance of moist energy for cloud formation; on the other hand, warm air advection stabilizes the boundary layer, cutting off those upward fluxes and preventing cloud formation. Generally, though, the relationship is complicated by other surface fields like the horizontal temperature gradient (Scott et al. 2020).

Finally, it is important to consider how the overturning circulation interacts with low cloudiness through the combined influence of other CCFs. For instance, Myers and Norris (2013) draw a connection between inversions and subsidence, whereby subsidence and stability mutually modify cloudiness across different regimes. They identify two ways in which they interact with cloudiness: first, under uniform subsidence, stronger inversions lead to decreased cloudtop height but increased prevalence of stratocumulus, while in uniform stability regimes, increasing subsidence leads to reduced prevalence and geometric height of stratocumulus cloudiness (Myers and Norris 2013). Physically, what happens in the second case is that as subsidence decreases, the boundary layer becomes deeper, leading to increased cloudiness within the layer as inversion strength remains invariant (Klein et al. 2017). Scott et al. (2020) also found that enhanced subsidence leads to a reduction of the outgoing shortwave from low clouds. However, recent observational analysis has generally deemphasized the role of subsidence in controlling tropical stratocumulus, as temperature

inversion strength and SST have been shown to be the dominant predictor of stratocumulus cloud fraction, their geographical characteristics, and observational estimates of the low cloud feedback (Scott et al. 2020; Myers et al. 2021; Cesana and Del Genio 2021).

Despite this, a recent study (Schiro et al. 2022) suggested that changes to the tropical overturning circulation might drive large changes to low clouds in response to greenhouse gas forcing in GCMs, contributing significantly to the intermodel spread in low cloud feedback. As the tropical overturning circulation is expected to weaken in response to greenhouse gas forcing, it has been suggested that this might lead to an increase in low cloudiness in the subtropical atmosphere (Myers and Norris 2013). Schiro et al. (2022) does in fact show that a greater slowdown of the tropical overturning circulation, as quantified by subsidence weakening, is linked to more low clouds in a warmer world. Generally speaking, however, the literature surrounding low cloud changes and explanations for the large intermodel spread in low cloud feedback is lacking in discussion of physical mechanisms dominating the responses. The way the pattern of sea surface temperatures evolve and the inter-model differences in these changes is thought to be a primary driver (Myers et al. 2023). Moreover, the modeled responses may be dissimilar from the expected responses based on observational analyses (e.g., Cesana and Del Genio 2021; Vogel et al. 2023). For instance, a recent study by Hill et al. (2023) found that GCMs are unable to reproduce the observed relationships between clouds and circulation and suggested that GCMs may be underestimating this component and consequently the total cloud feedback in the tropics. Identifying sources of model bias and their contribution to the intermodel spread is the central aim of this work.

Per unit area, stratocumulus have a much larger shortwave cloud radiative effect (CRE) (e.g., Tselioudis et al. 2021; Cesana et al. 2023), and thus most of the aforementioned studies on CCFs and low clouds have focused on stratocumulus clouds. Nevertheless, some evidence suggests the trade cumulus cloud feedback is also non-trivial (Myers et al. 2021; Cesana and Del Genio 2021), as

trade cumulus occupy a large fraction of the total tropical oceanic cloud landscape at any given time. Studying controls on tropical trade cumulus at both global and regional scales in observations and a hierarchy of models should, therefore, also be a top priority. Inter-model differences in the strength of the low cloud feedback have been linked to trade cumulus and their responses to greenhouse gas forcing in GCM studies across different generations and hierarchies of models (Bony and Dufresne 2005; Webb et al. 2006; Medeiros et al. 2008; Vial et al. 2013; Boucher et al. 2013; Medeiros et al. 2015), yet the mechanisms controlling this intermodel spread are poorly explained.

Cloud-circulation coupling in trade cumulus regimes is a critical gap in our knowledge of climate and climate change (Bony et al. 2017; Vogel et al. 2023). The community requires complementary analyses at larger scales (monthly, global) in satellite observations and GCMs to explore the relevance of small-scale processes to larger-scale climate changes. Vogel et al. (2023) is one such study that links small-scale process knowledge from field campaigns to large-scale climate feedbacks by evaluating the role of mixing between the boundary layer and free troposphere (Sherwood et al. 2014) as a potential control on low cloudiness, specifically in trade cumulus regimes. They conclude that while GCM low clouds are sensitive to the rate of lower tropospheric mixing, field campaign results suggest a weak relationship.

The overarching aim of my work is to contribute to the large-scale analysis of meteorological controls on both trade cumulus and stratocumulus in observations and GCMs to infer evidence of mechanistic relationships at larger scales that have been proposed from detailed cloud-resolving modeling and field campaign studies at smaller scales and the role of such mechanisms in contributing to the intermodel spread in climate sensitivity. This leads to two research goals:

- A. Through examining cloud-controlling factors for Sc and ShCu in observations, identify which CCFs are most important in determining cloudiness in the tropics, how these relationships vary regionally, and how they can favor one cloud type over

another. Quantify any changes to these clouds in response to meteorology, regional differences in these relationships, and the sensitivity of these results to the choices of datasets.

- B. Assess historical simulations of cloudiness across CMIP6 models to determine how consistently with observations these cloud-meteorology relationships are represented in models. Determine within which regions and to which CCFs low cloud sensitivity exhibits the largest biases in models.

To accomplish goal one, I am using two reanalysis datasets that provide meteorological variables and two satellite datasets that provide cloudiness information. To accomplish goal two, I use a historical model ensemble comprising 22 models and a pre-industrial control (piControl) model ensemble comprising 14 models. The latter ensemble is frequently used for cloud feedback studies because a satellite simulator is run inline with the model to output cloud fraction in a comparable fashion to how the satellites see the clouds. This allows for a more direct comparison between the modeled and observed clouds. Here, I use output from the ISCCP simulator, so our ISCCP observational results should be comparable to the ISCCP simulator output for certain relationships presented here, especially those that should not depend on the time period over which the analysis is performed or the exact forcing (such as the low cloud sensitivity to CCFs).

II. Chapter 1: Links between meteorology and tropical boundary layer cloudiness in observations

A. Data & Methods

Reanalysis data

a. NOAA OI SST V2

The NOAA 1/4° Daily Optimum Interpolation Sea Surface Temperature, version 2 (OI SST v2) dataset is hosted and maintained by NOAA's National Centers for Environmental Information. It blends ship- and buoy-based observations of sea-surface temperatures with observations derived

from the Advanced Very High Resolution Radiometer (AVHRR) sensor aboard NOAA weather satellites (Huang et al. 2021). In doing so, it provides an extensive record of SSTs (and a few other sea-surface based variables) dating back to the beginning of the satellite era, with data available on daily, weekly, and monthly bases from September 1981 to the present day (with a slight lag for data processing and input). This invaluable data is on a $0.25^\circ \times 0.25^\circ$, or 1440×720 , grid, covering the globe at a single level. In this study, I use it as the sole observational sea-surface temperature dataset, regridded to the $2.5^\circ \times 2.5^\circ$ grid of the satellite data, in lieu of the MERRA-2 and ERA-5 reanalysis SST fields. I also use this dataset as the observational dataset for global surface temperature changes. Although this dataset does not capture land surface temperature, using a global mean sea-surface temperature quantity is in line with previous literature which has examined CCF-cloud relationships.

b. MERRA-2

Monthly mean reanalysis data used for compositing cloud data with meteorological variables was sourced from NASA's Modern Era Retrospective analysis for Research and Applications, version 2 (MERRA-2) (Gelaro et al. 2017). These data were retrieved from NASA's Goddard Earth Science Data and Information Services Center (GES DISC) and include air and sea-surface temperature, relative humidity, surface (10 m) wind speed, and pressure vertical motion (ω), among others, at 31 pressure levels along a $.5^\circ \times .625^\circ$ latitude by longitude grid. The data was re-gridded to be on the $2.5^\circ \times 2.5^\circ$ grid of the observational satellite data and finally had land masked out so that our analysis reflects processes above the ocean only. The time-average mean of each CCF in the set, along with the NOAA OI SST product, is shown in Figure 1.

c. ERA-5

Supplemental monthly mean reanalysis data for sensitivity testing was from the European Center for Medium Range Weather Forecasting's (ECMWF) Reanalysis v5 (ERA-5) (Hersbach et al. 2020). This was retrieved from ECMWF's Copernicus Data Service web service with the same

interested quantities as in MERRA-2. ERA-5's grid is finer than MERRA-2's, at $.25^\circ \times .25^\circ$, and it is resampled to the same $2.5^\circ \times 2.5^\circ$ grid as in the satellite observations. For illustrative purposes, the difference between each MERRA-2 and ERA-5 CCF (calculated by subtracting ERA-5 values from MERRA-2 values) is displayed in Figure 2.

d. Derived statistics

Beyond the basic atmospheric information within reanalysis, I derived a handful of additional quantities. First, I derived estimated inversion strength (EIS), a measure of the change in the moist profile in the lower atmosphere as a linear combination of lower tropospheric stability (LTS; the difference between the potential temperature at 700 hPa and the surface) and the lapse rate between the surface and lifting condensation level (LCL) (Wood and Bretherton 2006). From the zonal and meridional wind data provided in reanalysis, I also derived a single wind speed (WS) vector that is simply calculated as the Euclidean norm of the two wind components. Finally, I derive temperature advection from the surface wind speed components and surface air temperature using the dot product of the wind and temperature gradient vectors. The full equations are given below.

$$EIS = LTS - \frac{g}{c_p} \left[1 - \frac{1 + \frac{L_v q_s}{R_a T}}{1 + \frac{L_v q_s}{c_p R_v T^2}} \right] (z_{700} - z_{LCL}) \quad (\text{Wood and Bretherton 2006}) \text{ Eq. 1a}$$

g is the gravitational constant (9.8 m s^{-2}), c_p is the specific heat of air at constant pressure (1005.7 J kg^{-1}), L_v is the latent heat of vaporization of water, q_s is the saturation mixing ratio, R_a and R_v are ideal gas constants for dry air ($287.04 \text{ J kg}^{-1} \text{ K}^{-1}$) and water vapor ($461.5 \text{ J kg}^{-1} \text{ K}^{-1}$), respectively. z is the geometric height of each pressure level in meters, derived from pressure and temperature using a logarithmic decrease of pressure assumption for z_{700} and Lawrence (2005)'s method for z_{LCL} as

communicated by Romps (2017), where

$$z_{LCL} = \left(20 + \frac{T - 273.15 \text{ K}}{5 \text{ K}} \right) (100 \text{ m}) (1 - RH_{sfc}) \text{ Eq. 1b}$$

and RH_{sfc} is the surface relative humidity. In some studies, this is taken to be a constant .8 based on the climatology of marine relative humidity, but I use the true local relative humidity (Wood and Bretherton 2006). Due to the relative novelty of this method for calculating LCL, there are comparatively few studies which utilize it and fewer still which use it to calculate EIS. Because of this, there are no comparative studies which examine different methods of calculating EIS that include this method, which may explain for some of the differences between my results and other published climatologies of EIS, and indeed the relationships drawn thereupon.

$$WS = \sqrt{u^2 + v^2} \text{ Eq. 2}$$

u is the east-west (zonal) component of the surface wind, and v is the north-south (meridional) component of the wind.

$$T_{adv} = -u \frac{\partial T}{\partial x} - v \frac{\partial T}{\partial y} \text{ Eq. 3}$$

u and v retain their definitions from equation 2; ∂T is the finite difference between temperatures at two points; and ∂x and ∂y are the finite distances between two gridpoints in the east-west and north-south directions, respectively.

Satellite data

a. ISCCP

The International Satellite Cloud Climatology Project (ISCCP) makes use of routine observations by operational weather satellites to provide a long-term (1983-2018), gridded, global record of cloud properties. ISCCP uses observations in the visible and infrared window portions of the spectrum to determine cloud optical thickness and cloud top temperature, from which the cloud top pressure is inferred. ISCCP version 20130503 monthly means have been taken from Lawrence-Livermore National Laboratory's Observations for Model Intercomparisons project (Schiffer and Rossow 1983, Teixeira et al. 2014). The data is along a $2.5^\circ \times 2.5^\circ$ latitude by longitude grid with 7

pressure levels and 6 optical thicknesses, from January 1997 through June 2008. There is a single cloud fraction variable from which multiple cloud types can be distinguished using various bins in cloud top pressure and optical depth space, following the classification histogram found on NASA's ISCCP website. Using this method allows for three different types of cloud classifications: first, the common name for a cloud type, like cumulus, cirrus, and stratus; second, by level regardless of thickness, like low, medium, and high; and third, by level with an additional parameterization for thickness, like low and thick or high and thin. In this project, the low cloudiness definition used is the total cloudiness between the surface and 680 hPa, summed across all optical thicknesses. This provides a broad look at all boundary layer cloudiness across regimes. This data serves as the secondary dataset in this experiment for comparison with CASCCAD data.

b. CALIPSO-CASCCAD

Expanding on the idea of dividing clouds by physical characteristics into subgroups based on cloud species or height and thickness, the Cumulus And Stratocumulus CloudSat-CALIPSO Database (CASCCAD) project further seeks to define types of low clouds using more advanced satellites than were available to ISCCP: CloudSat and CALIPSO, which were both launched in April of 2006 (Cesana et al. 2019). CASCCAD is a hybrid product using CloudSat's cloud profiling radar and CALIPSO's lidar. In combining these products, CASCCAD is specifically meant to resolve low clouds. These data include a dozen cloudiness masks on a $2.5^\circ \times 2.5^\circ$ grid, including low cumulus and stratocumulus clouds (NASA GISS). They were downloaded through correspondence with G. Cesana over a period covering 01-2007 to 12-2015 on a monthly average basis at a single level and were processed with the same land mask as the other data to provide only oceanic scans. There are two key cloud definitions contained within the CASCCAD set: low cumulus, variously referred to as "trade" or "shallow" cumulus, defined as Cu clouds with a height above 1.92 km and terminating below 3.36 km, and stratocumulus, defined based on having a height below 1.92 km, a horizontal

extent greater than a certain threshold based on four different length scales, and how the cloudiness is structured in the vertical (i.e., no Cu below the Sc deck) (Cesana et al. 2019; NASA GISS). Per the U.S. standard atmosphere of 1976, this provides that shallow cumulus clouds have a maximum height of 670 hPa, and that stratocumulus clouds have a maximum height of 800 hPa, both of which are consistent with the ISCCP low cloudiness definition above.

Maps of low cloud fraction climatology for Sc and ShCu and ISCCP low cloud fraction are shown in Figure 3. Superimposed on each panel is the climatological boundary where CASCCAD depicts the ratio of stratocumulus cloudiness to the sum of stratocumulus and shallow cumulus as being 50%. The CASCCAD Sc product in the top panel shows that the detection of Sc clouds is heavily restricted to either outside the tropics or in the eastern basins of oceans, with the latter greatly outweighing the former and being tightly concentrated. In the center panel, the CASCCAD ShCu signal is overall weaker than the Sc signal, with maxima around thirty percentage points lower than the corresponding Sc maxima. Geographically, the core regions that ShCu are found in are open oceans between regions where Sc dominate and deep convection dominate. For example, in the Pacific, the primary ShCu belt occurs approximately halfway between Oceania and South America, stretching from approximately Easter Island through to northeastern French Polynesia. In the final panel, the total ISCCP low cloudiness bears similarity to CASCCAD's stratocumulus product, highlighting cloudiness in the cores of those eastern ocean basins, and showing moderate skill at capturing cloudiness in shallow cumulus regions, though there are also some very important differences. Primarily, ISCCP picks up on mid and high latitude low cloudiness much more than CASCCAD, with broad and intense banks of cloudiness stretching along the southern fringes of the Indian and Pacific and around Kamchatka through the Aleutian Peninsula. For the purposes of this study, however, we will remain focused on the tropics.

Using the Sc and ShCu data in the CASCCAD dataset, we can construct geographic boundaries which nicely divide the tropics into two regimes: one which is dominated by shallow cumulus, and one which is dominated by stratocumulus. This can be applied to maps, for quick visual analysis, or used analytically to create domain averages for any data. The formula is simple:

$$b = \frac{ShCu}{ShCu + Sc}$$

By taking the time average across the whole CASCCAD series, we are provided with a single contour which divides cloudiness such that values of b less than 50% are Sc-dominated, and values of b greater than 50% are ShCu-dominated. This methodology is calqued from Cesana et al. 2023, and the boundary is displayed on many of the figures in this study. To refine their method for our purposes, we calculate shallow cumulus regional means only in grid cells that experience 500 hPa subsidence at every time step in ERA-5 in order to exclude relationships that are reflective more of deep convective regimes.

Regression analysis

In both chapters of this paper, I heavily utilize both simple and multiple linear regressions. These are calculated using the Pingouin Python package. For both regressions, each individual CCF is standardized by the ERA-5 tropics-only standard deviation from mean. This standardization serves a dual role: first, it allows for simple comparison between quantities which may hold vastly different values – for example, relative humidity is between 0 and 1, while vertical motion may be in the hundreds of hPa per day. Its second purpose is to both emphasize the tropics in my analysis by reducing the impact of extratropical signals. In simple regressions, the standardized values are then regressed against the latitudinally weighted global mean surface temperature at each gridpoint so that the final product is a 72 x 144 map of regression coefficients. In the case of multiple linear regression, the cloud fraction quantity of interest (Sc, ShCu, or ISCCP LCF) is regressed onto all six

of the CCFs, providing coefficients that fulfill the equation $Y = b_1x_1 + \dots + b_6x_6 + \epsilon$, with b_n being the n^{th} coefficient and epsilon being an error term. The reason that multilinear regression is used for cloud-CCF relationships instead of a simple linear regression is that these relationships tend to be collinear, so we can remove undue influence on (for example) temperature advection by wind speed from the model.

B. Results

Relationship of cloudiness to meteorology

To set the stage for analysis of cloud-CCF connections, we should first understand how those meteorological factors respond to interannual warming and changes in the global mean sea-surface temperature. In Figure 4, we see the simple linear regression coefficients for each MERRA-2 CCF regressed onto the time series of NOAA OI global mean SSTs (T_s), as well as NOAA OI SSTs onto T_s . Except in the north Pacific and along the ITCZ, EIS is generally positively related to increases in surface temperature in the tropics; interestingly, the northern Pacific zone of decrease hews very closely to stratocumulus cloudiness, while other Sc regions follow the general strengthening found through the rest of the tropics. RH is reduced throughout much of the tropics except in the Indian ocean and central Pacific, mirroring the pattern of circulation changes (stronger subsidence corresponding to a RH reduction). Subsidence is slightly increasing in stratocumulus regions in the southern hemisphere and in the southern part of the northeast Pacific but is reducing in the central-eastern Pacific and in some parts of the northern hemisphere. Additionally, the trade winds weaken in the deep tropics along the ITCZ in the central Pacific, with inconsistent strengthening and weakening patterns elsewhere. Temperature advection only notably changes about the ITCZ in the Pacific, where it increases, and in the southeastern Pacific Sc bank, where it decreases. SST increases along the equator in the Pacific when global mean SSTs increase, suggesting that global temperatures rise during El Niño events. The ERA-5 results are mostly very similar in

spatial pattern to the MERRA-2 results, with a key exception: each response appears to be of a larger magnitude than the corresponding relationship in MERRA-2. In summary, however, the domain average of the 5 non-EIS CCFs are roughly on par with their MERRA-2 counterparts, generally being no more than a few tenths of a standard deviation per Kelvin away. Given the similarity in spatial distributions and summary statistics, these results are not shown.

Importantly, note that the patterns and magnitudes of these CCF responses to global mean surface temperature increases will depend on the time period chosen for the analysis. Here, I analyze a time period of 2007-2015 corresponding to the CASCCAD observations, though other studies have noted differences in $dCCF/dT_s$ and $dLCF/dT_s$ depending on the time period analyzed (Cesana and Del Genio 2021). I do not, however, expect $dLCF/dCCF$ relationships to change much as a function of time period being analyzed. Though $dLCF/dCCF$ sensitivity to the historical time period was not analyzed, nonstationarity in $dLCF/dCCF$ was briefly explored as a part of this project comparing $dLCF/dCCF$ in the historical record to $dLCF/dCCF$ in an anthropogenically warmed future and was found to be trivial (not shown).

Now, I will assess the sensitivity of the low cloud fraction to changes in these cloud controlling factors to consider how these meteorological responses to surface warming may affect the cloudiness. Beginning with stratocumulus cloudiness, we first look to Figure 5, which shows the multiple linear regression coefficients between CASCCAD's Sc cloudiness and MERRA-2's CCFs. In stratocumulus areas, Sc cloudiness increases in response to increased stability, RH_{700} , subsidence (though noisily), and surface wind speed, and decreases sharply in response to increased sea surface temperatures and temperature advection. These Sc zone signals are generally consistent regardless of basin, except for RH_{700} , which decreases cloudiness in the northeast Pacific. The ERA-5 results are similar to the MERRA-2 results (Figure 6), with a few exceptions: the sensitivity of Sc to EIS is enhanced and the sensitivities of Sc to SST and T_{adv} are substantially reduced. Comparing the

ISCCP analysis of dLCF/dCCF in Figures 7 and 8 to CASCCAD Sc dLCF/dCCF in Sc-dominant regions reveals that dLCF/dEIS is reduced in the ISCCP analysis. dLCF/dT_{adv} is larger in the ISCCP/ERA5 analysis than in the CASCCAD/ERA5 analysis. Finally, following the methodology of Naud et al. (2023), the maximum regression coefficient among all six CCFs for the CASCCAD regression with both MERRA2 and ERA5 reanalyses are plotted in Figure 16. In both reanalyses, Sc are dominantly controlled by EIS, with the ERA5 analysis suggesting the critical importance of RH at the Sc-ShCu transition margins in the SE Pacific and SE Atlantic.

Next, I analyze the CASCCAD ShCu sensitivities to the same six CCFs. This analysis reveals important relationships underpinning meteorological controls on the transition from Sc to ShCu. First, decreases in EIS, RH₇₀₀, and ω_{700} and increases in T_{adv}, SST, and WS will generally favor ShCu at the expense of Sc on the fringes of the Sc regions. Slightly further away from these transition regions where ShCu are more prevalent (recalling Figure 3), the relationships sometimes switch signs in certain regions: for instance, lower SSTs and higher EIS end up favoring ShCu in dominant ShCu region of the SE Pacific. However, these relationships are not the same everywhere. Comparing across the MERRA2 and ERA5 results, the relationships are quite similar, which is summarized in Figure 18.

Connecting cloudiness to temperature through meteorology

Having outlined the relationships between MBL clouds and meteorology and meteorology to interannual warming, I now examine how temperature change influences boundary layer cloudiness when mediated by meteorology. Figure 10 shows the calculated product of the regression coefficients between Sc cloudiness and CCFs and CCFs and mean surface temperatures in NOAA OI, which constitutes the quantity $\frac{\partial Sc}{\partial CCF} \frac{\partial CCF}{\partial T_s}$ for each individual CCF. Because this is a simple product, many of the characteristics of the two terms are propagated directly through the calculation and are easily identifiable, while still creating unique signals of their own.

Far and away, the two CCFs with the strongest relation to Sc are SST and EIS. Their coefficients are both spatially cohesive and high in magnitude, with their stratocumulus regional means both in excess of $\pm 4.0\% \text{ K}^{-1}$. EIS increases Sc throughout much of the tropical Pacific and Atlantic, except in the NE Pacific and along the equator where the opposite occurs: EIS decreases Sc cloud fraction. Through SST, cloudiness sharply decreases. The remaining four CCFs contribute relatively little to the total change in Sc cloud fraction. Temperature advection is the exception here, with an area of strong coefficient products centered directly in the heart of the southeast Pacific stratocumulus zone which overlies the strongly negative SST and strongly positive EIS responses, potentially tipping the scales just enough so that the mean response of Sc to Ts over this time period (2007-2015) is actually positive in this region. In ERA-5, these results are largely the same, seen in Figure 11, as should be expected given the similarities of their constituent parts.

To infer the total response of cloudiness to interannual warming, there are two avenues we may follow: by directly calculating a $\frac{DLCF}{DT_s}$ quantity, or by reconstructing it through the individual regressors in our model, i.e. by calculating $\frac{DLCF}{DT_s} = \sum_{i=1}^6 \frac{\partial LCF}{\partial CCF_i} \frac{\partial CCF_i}{\partial T_s}$. Of course, these two quantities will not be perfectly equal. Not only does error compound with each subsequent calculation, the six CCFs that we use are unlikely to completely represent the state of forcings that influence cloudiness. So, in using both of these quantities in conjunction with the products above, we can determine which CCFs translate the most influence from warming to cloudiness. Figure 12 shows both of these methods calculated for both sets of reanalysis data and CASCCAD Sc. What is immediately obvious across all four panels is that southern hemispheric Sc cloudiness increases in all three primary basins off the coasts of Perú, Angola, and Australia and that it decreases in the northern hemispheric basins off the coasts of California and Morocco/Iberia. This is probably due to the time period chosen for the analysis and the resulting sea surface temperature pattern, as this is

not seen in other studies illustrating $dLCF/dT$ s over the historical record (Cesana and Del Genio 2021; Myers et al. 2023). Looking back to Figures 10 and 11, it appears that the positive influences by EIS and T_{adv} on Sc cloudiness outweigh the reduction that SST brings in the southeast Pacific, while in the northeast Pacific, the lack of EIS' cloud-increasing influence allows SSTs to dominate and reduce stratocumulus cloudiness. There are also substantial decreases along the ITCZ. The differences between the various east ocean stratocumulus regimes are, to a point, enigmatic. Furthermore, the reconstructions show $dLCF/dT$ s of smaller magnitude compared with that from the direct calculation, evidenced by both the weaker domain averages and the lower saturation points of the colorbars associated with the reconstructions. This suggests that nonlinearities exist in these relationships that are not adequately captured by the methods employed here. It may also suggest that there are important meteorological predictors that are missing from our MLR.

We may examine the response of trade cumulus cloudiness to interannual warming utilizing the same techniques as above; shown in Figure 9 are the multiple linear responses of ShCu cloudiness to the six CCFs in MERRA-2. Again, the MERRA-2 results generally show stronger relationships than the ERA-5 results. In ShCu regions, stronger EIS generally supports an increase in ShCu cloud fraction in response to warming, though this depends on the region. Nearer to the edges of the Sc regions, a decrease in EIS supports increases in ShCu cloud fraction in response to warming. In the heart of Sc zones, increasing EIS generally acts to decrease shallow cumulus cloudiness in response to warming, though this relationship is regionally dependent. Wind speed decreases in response to warming reduce ShCu fraction along the equator. RH_{700} changes act to enhance ShCu fraction along the central Pacific, in the north Pacific near Hawai'i, and in the S Pacific along the south Pacific Convergence Zone region. Changes in temperature advection decrease ShCu in the S Pacific, but generally have a small influence on ShCu changes in response to warming in most regions. Finally, SST and subsidence contributions to ShCu changes with

increasing T_s are fairly noisy, though increases in SST support an increase in ShCu in Sc-ShCu transition regimes. The ERA-5 results do not differ significantly anywhere besides being weaker overall, and so have been omitted.

By once again inspecting the sum of the products in the prior paragraph as a reconstruction of $\frac{DShCu}{DT_s}$ as well as the directly calculated quantity, we may properly determine the connections between surface temperature and ShCu cloudiness with meteorology acting as an intermediary. This is depicted in Figure 15, which again shows the reconstructed and directly regressed linear regression coefficients between CASCCAD shallow cumulus cloudiness and each reanalysis' global mean surface temperature. All four are quite consistent across the tropics, mainly differing in magnitude: the reconstructions are around half the strength of the direct calculations, and the background values in the reconstructions are much closer to zero, driving their averages down in comparison to the single regression between ShCu and T_s . What these plots suggest is that interannual warming is acting to decrease shallow cumulus cloudiness in regions like the south central Pacific, southwest Atlantic, and central to southern Indian which in the observational record are hotspots for shallow convection and increasing it in certain other regions. Most notably, this includes along the eastern Pacific ITCZ, slightly branching into the southeast Pacific subsidence zone, and the northeastern Pacific stratocumulus basin. Increases along the EPac equatorial zone and in the NE Pacific are likely signifying a regime shift from Sc to ShCu in response to warming surface temperatures. Rising sea-surface temperatures are the primary reason for an increase in ShCu in the NE Pacific (Figure 17), with decreases in wind speed and increased warm advection decreasing ShCu in the central Pacific. In ascent regions, such as near the Maritime Continent, in the tropical west Pacific and in the Indian oceans, increased EIS increases the ShCu. A decrease in RH_{700} in the central N/S Pacific straddling the equator acts to reduce the decrease in LCF there, as this decrease in RH_{700} acts to increase ShCu.

C. Discussion

As the atmosphere and oceans continue to warm due to anthropogenic greenhouse gas emissions, the cloudscape will fluctuate in its response both to warming and to local meteorological parameters which are reshaped by this warming. Consider the northeast Pacific, between Hawai'i and Central-North America. Reanalyses indicate that the atmosphere above it is destabilizing in the lowest 300 hPa by around 2.0 standard deviations of EIS per Kelvin of warming, and that its surface waters are warming by anywhere from 2.0 to 3.0 standard deviations per K of global warming. These changes are anathema to stratocumulus cloudiness, which historically dominates the region due to the broad oceanic upwelling that occurs there. These are the dominant meteorological changes driving Sc reduction in the NE Pacific, as shown in Figure 18. Moisture at the interface between the MBL and the free troposphere and temperature advection are also important facets for the formation of Sc cloudiness, though these changes are occurring at a relaxed rate compared to EIS and SST. As these CCF changes occur, it appears that shallow cumulus cloudiness in the region is increasing at the expense of Sc cloudiness. Because reduced lower tropospheric stability (EIS) and free tropospheric humidity and heightened sea surface temperatures are seemingly prerequisites for shallow cumulus convection, these changes are paving the way for a regime shift, from stratocumulus cloudiness to trade cumulus clouds. However, this decrease in clouds and the regime shift from Sc to ShCu is not noted in every region.

To better understand why the northeast Pacific Sc zone reacts differently to warming in comparison to others, a useful exercise could be to determine how the regions themselves differ and how climatological differences might sway these regressions. Meteorologically, the different regions share many similarities: high EIS, subsidence, and surface winds, with low SST, T_{adv} , and RH_{700} , referring back to Figure 1. Stratocumulus cloudiness itself seems slightly more frequent in the southeast Pacific and Atlantic in comparison to the NE Pacific, but only by a few percentage points.

However, the degree to which the climatology differs among the regions and how this affects the cloud changes noted, however, is beyond the scope of this study. Moreover, we expect that the north-south Pacific dipole pattern of change shown in Figure 12 is largely determined by the time period analyzed in our experiment and is not largely representative of multi-decadal trends in LCF in response to increasing greenhouse gases (Cesana and Del Genio 2021; Myers et al. 2023).

Figures 16 and 17 show which CCF has the highest absolute multiple regression coefficient with Sc and ShCu, respectively, at a given gridpoint, which serves as a proxy for the “importance” of each CCF because of their being standardized. Beginning with Figure 16, we see that the two reanalysis products broadly agree on which CCF most influences Sc cloudiness throughout the tropics, with EIS dominating. The primary difference between the two is that ERA-5 favors RH₇₀₀ slightly more in the southeastern Pacific, around 20°S, where MERRA-2 favors humidity in only a smattering of grid cells. The equivalent plots for ShCu clouds (Figure 17) are quite similar across reanalyses, to about the same degree as Sc clouds, though they do vary more in space. In shallow cumulus dominated regions, wind speed is the strongest control, with temperature advection being more important in transition zones between ShCu and Sc domains. In ShCu regions, these plots indicate that the most important CCF differs depending on the location: in the SE Pacific, a blend of T_{adv}, WS, and SST contribute the most to the multiple regression model, while in the NE Pacific, SST dominates. For the most part, EIS is absent, except in regions of strong ascent with frequent deep convection. In other words, Sc and ShCu can have different dominant CCFs, and the dominance of a certain CCF for ShCu depends greatly on the region.

To our knowledge, our study is the first to document relationships from the six CCFs (EIS, SST, RH₇₀₀, ω_{700} , WS, and T_{adv}) to Sc and ShCu from the CASCCAD data products. ShCu relationships to CCFs, in particular, are not well-documented in the literature, in large part due to the challenges associated with characterizing the distinct shallow cloud types using satellite data.

Moreover, many studies use stability or large-scale dynamical variables to separate out Sc and ShCu regimes across the tropics without actually assessing the differences in relationships between CCFs and the different cloud types, as multiple cloud types can co-exist within a given region. This new CASCCAD dataset, however, shows promise in distinctly characterizing Sc and ShCu, permitting us to distinctly characterize ShCu-CCF and Sc-CCF relationships. This is especially useful in Sc-ShCu transition regimes where such an analysis has been particularly difficult and is often only accomplished using field campaign data or large eddy simulations.

Finally, I consider the potential impacts that variations and discrepancies between the various datasets can have on drawing conclusions about low cloud sensitivities to CCFs and thus to surface warming. If we compare the mean meteorological states of each reanalysis (Figure 2), EIS, subsidence, relative humidity, and 10 meter wind speed are each weaker in core tropical boundary layer cloud regions in MERRA-2's climatology, which leads to the question of "how might a weaker representation of a signal impact the analysis performed on it?" Disregarding that certain facets of the signals may be similar even though their amplitudes are not alike, like frequency, we can suppose that an on average weaker dependent variable in a linear regression will lead to a weaker linear relationship and thus a smaller regression coefficient. So, working from that assumption, it seems appropriate that Figures 4 and 5 show just that: weaker responses in MERRA-2 CCFs to SSTs than in ERA-5 CCFs. Inspecting multiple linear cloud-meteorology relationships reveals that CASCCAD and ISCCP cloudiness are each more dependent on MERRA-2's meteorology than they are on ERA-5's, i.e., their regression coefficients are greater in response to MERRA-2 than they are to ERA-5. However, this leads to their products each being on similar magnitudes. Therefore, depending on the use intended for the data, it is important to consider these biases — for example, if calculating the products of CASCCAD-MERRA-2 and MERRA-2-SST and vice versa for ERA-5 to determine the cloud response to warming through meteorology, as was done in this study, the

choice may be less critical than if observations of $dLCF/dCCF$ are used to constrain modeled relationships.

D. Conclusion

Per observations, the meteorological parameter that provides the most control over tropical stratocumulus cloudiness is EIS, with certain regionally-dependent contributions from RH_{700} and SST (Figure 16). This is broadly consistent with the existing literature's conclusions on MBL cloudiness and meteorology, recalling in particular those of Scott et al. (2020), Myers et al. (2021), and Cesana and Del Genio (2021). However, this is not the case for shallow cumulus cloudiness: in the open ocean trade wind basins, ShCu clouds are largely controlled by wind speeds, with EIS and SST only exceeding the influence of wind speed in the margins surrounding ShCu regions. EIS dominates to the west of shallow cumulus regions, while SST and T_{adv} dominate to the east. These relationships are less well documented in the literature on a global scale. In summary, there are large differences between Sc and ShCu clouds and their relationships to local meteorological perturbations.

The different cloud types respond differently to warming (Figures 12 and 15) due to (a) differences in dominant meteorological controls (Figures 16 and 17) and (b) differing responses of the Sc and ShCu to CCFs (Figures 10-11, 13-14). Moreover, as is especially true for ShCu, the dominance of a certain CCF on ShCu depends greatly on the region (Figure 17), and thus the CCF contributing the most to the total $dShCu/dT$ s varies regionally (Figure 18). Moreover, these results suggest that the ShCu cloud feedback may be more sensitive to RH_{700} , wind speed, and temperature advection than other studies have suggested, based on their analysis of $dShCu/dCCF$ averaged over broad geographical regions (Cesana and Del Genio 2021). This work thus suggests the importance of retaining information about regional variability in $dLCF/dCCF$ and more holistically considering controls on the low cloud feedback, especially for the trade cumulus feedback.

Additionally, since a common approach to observationally constraining the low cloud feedback is to multiply observed cloud-CCF relationships with modeled CCF-Ts relationships, I caution that this process could be non-trivially affected by the choice of reanalysis and cloud dataset. My results suggest that using a variety of observational products to perform such an exercise is best practice. In particular, using a dataset like CASCCAD to better distinguish Sc from ShCu could help to more clearly define the contributions of Sc and ShCu changes to the total cloud feedback, compared with popular methods that define ShCu regions/feedbacks solely based on EIS and large-scale dynamical metrics.

Finally, that the direct calculation of $dLCF/dT_s$ is much larger than the sum of the $dLCF/dCCF * dCCF/dT_s$ terms for all six CCFs suggests that there may be CCFs missing from the linear model and/or there are nonlinearities in the system that are important to the prediction of low cloud fraction. Examining nonlinearities using machine learning could be one fruitful avenue of future research.

III. Chapter 2: Representation of links between meteorology and tropical boundary layer cloudiness in models

A. Data and Methods

Historical simulations

For the historical models, there are 22 in total, all from the Coupled Model Intercomparison Project, Phase 6. These models were on grids which varied widely, and so all were regridded to a standard 142×192 $1.25^\circ \times 1.875^\circ$ grid to match the first model in the set alphabetically (ACCESS-CM2). These datasets each contain the following 4-D variables: pressure vertical motion, temperature, relative humidity, and zonal and meridional wind speeds. The single level variables are a consolidated ISCCP simulator low cloud fraction product, zonal and meridional wind speeds at 10

meters, and temperature at 10 meters. The historical data represents the period 2000-01 through 2014-12. Below in Table 1 is a list of models used:

Model Name	Grid Size
ACCESS-CM2	1.25° x 1.875°
ACCESS-ESM1-5	1.2414° x 1.875°
BCC-CSM2-MR	1.125° x 1.125°
CAMS-CSM1-0	1.125° x 1.125°
CanESM5	2.8125° x 2.8125°
CESM2-WACCM	0.9375° x 1.25°
CMCC-CM2-SR5	0.9375° x 1.25°
CMCC-ESM2	0.9375° x 1.25°
CNRM-CM6-1	1.4062° x 1.4062°
CNRM-ESM2-1	1.4062° x 1.4062°
FGOALS-f3-L	1.0° x 1.25°
FGOALS-g3	2.25° x 2.0°
GFDL-ESM4	1.0° x 1.25°
MIROC6	1.4062° x 1.4062°
MPI-ESM1-2-HR	0.9375° x 0.9375°
MPI-ESM1-2-LR	1.875° x 1.875°
MRI-ESM2-0	1.125° x 1.125°
NESM3	1.875° x 1.875°
NorESM2-LM	1.875° x 2.5°
NorESM2-MM	0.9375° x 1.25°
TaiESM1	0.9375° x 1.25°
UKESM1-0-LL	1.25° x 1.875°

Table 1: Model names and original grid sizes for each of the 22 historical (2000-01 – 2014-12) models.

Pre-industrial control simulations

To supplement the historical and future simulations and provide comparisons for sensitivity, we also procured 14 pre-industrial control (piControl) model runs. They represent a 10 year period which assumes the concentration of CO₂ in the atmosphere is held constant at a pre-industrial mean level of around 280 ppm, representative of conditions prior to the anthropocene. There are no anthropogenic or volcanic sources of carbon dioxide in the models, so the concentration is constant for the whole run (Eyring et al. 2016). The ensemble comprises 10 CMIP6 and 4 CMIP5 models, all regridded to the 1.25° x 1.875° resolution that the historical models were regridded to. In this ensemble, the cloudiness product is an ISCCP simulator, which mimics cloudiness as the real ISCCP constellation would perceive it. To account for overlap issues that may arise when high and low cloudiness are depicted in the same grid cell, I define low cloudiness in these models with the following equation:

$$Adj.LCF = \frac{LCF}{1 - HCF - MCF}$$

where LCF is the ordinary low cloudiness between the surface and 680 hPa across all optical thicknesses, HCF is all cloudiness above 440 hPa, and MCF is all cloudiness between the two levels. Without performing this adjustment, the regressed relationships between vertical motion and low cloudiness would be inaccurate because of the ties between vertical motion and high cloudiness in the tropics. The 14 models, their original resolution, and their CMIP phase are listed in Table 2 below.

Model Name	Grid Size	Model Generation
CanESM5	2.8125° x 2.8125°	CMIP6
CNRM-CM6-1	1.4062° x 1.4062°	CMIP6
CNRM-ESM2-1	1.4062° x 1.4062°	CMIP6
E3SM-1-0	1.0° x 1.0°	CMIP6

E3SM-2-0	1.0° x 1.0°	CMIP6
E3SM-2-0-NARRM	1.0° x 1.0°	CMIP6
IPSL-CM5A-LR	1.875° x 3.75°	CMIP6
IPSL-CM5A-MR	1.2587° x 2.5°	CMIP6
IPSL-CM6A-LR-INCA	1.2587° x 2.5°	CMIP6
MIROC-ES2L	2.8125° x 2.8125°	CMIP6
MIROC5	1.4062° x 1.4062°	CMIP5
MIROC6	1.4062° x 1.4062°	CMIP5
MPI-ESM-LR	1.875° x 1.875°	CMIP5
MRI-ESM2-0	1.125° x 1.125°	CMIP5

Table 2: Model names, original grid sizes, and CMIP generation for each of the 14 piControl models.

Regression analysis

The regression analysis in this chapter is identical to that performed in the first chapter, with ERA-5 observations serving to standardize the data, but with the additional facet that we may examine the responses across models. This opens many avenues: we may look at the average response across all the models; regional means of regression coefficients per model; standard deviation of responses across models, in order to assess model spread. The latter two routes allow us to see which areas and variables contribute the most to model spread in model uncertainty in low cloudiness, which could ideally help pinpoint a non-trivial source in spread in modeled climate sensitivity.

B. Results

Relationship of cloudiness to meteorology

We begin by determining the relationships that meteorological characteristics take on with interannual warming. Figure 19 shows the historical simple regression response in EIS, RH_{700} , ω_{700} ,

SST, T_{adv} , and surface wind speed in standard deviations per Kelvin. These spatial patterns and those shown for piControl in Figure 20, are quite similar to both sets of reanalysis data. The only major difference among the simulations is that the response of EIS to T_s is larger in magnitude in the historical simulations than in piControl.

If we look at the sensitivity of the low clouds to CCFs in the models, shown in Figure 23, we see similar relationships to those presented in our observational analysis, with some noteworthy exceptions. In summary, the six CCFs uniformly influence cloudiness across the globe in the following ways: EIS increases cloudiness, doing so at an increased rate in Sc zones; RH_{700} increases cloudiness, at heightened levels in southern hemispheric Sc regions, with little to no relationship in the heart of stratocumulus regions; increased ω_{700} (subsidence) decreases LCF everywhere other than in southern hemispheric Sc zones; SST decreases cloudiness besides directly in the core of the SE Pacific and Atlantic. Note that the ω_{700} being broadly anticorrelated with low cloud fraction across the tropics is consistent with the observational results presented in Scott et al. (2020) but is not supported by the observational results presented in this study. Temperature advection and wind speed are both slightly more spatially varied than the others: T_{adv} generally decreases cloudiness except in certain ShCu regions (consider the south central Pacific and southwest Atlantic) and in the heart of stratocumulus regions. The models show spatially varying relationships between wind speed and stratocumulus. The sensitivity of LCF to T_{adv} and WS is greatly reduced in the model ensemble in comparison to the observations, while the sensitivity of LCF to ω_{700} , RH_{700} , EIS, and SST is generally stronger. Note that the greater sensitivity of modeled low clouds to vertical velocity was also noted in Grise and Kelleher (2021), as was a reduced sensitivity of models to T_{adv} .

Turning to the piControl ensemble, which should be the most comparable to the ISCCP observational analysis as the ISCCP satellite simulator was used to output the cloud fraction in the ensemble members chosen for the analysis, the results are somewhat different from these historical

regressions. Shown in Figure 25, there are some broad signatures identifiable in a way similar to the historical ensemble, with the overall backgrounds of EIS, RH_{700} , SST, T_{adv} , and WS each generally matching their historical counterpart – that said, there is much more variation embedded within those background characteristics than in the historical relationships. Within the tropics, EIS is a more positive influence on cloudiness than in the historical simulations, with those positive signals peaking in certain ShCu areas and extending into the outlying western areas of Sc. RH_{700} still generally increases cloudiness, though this relationship disappears within ascent regions. ω_{700} is entirely different from the historical ensemble results, appearing as a positive regression coefficient almost worldwide (whereas the historical models were negatively related to increased subsidence), with only a few regions on the poleward sides of Sc regions having negative relationships. These relationships, however, appear to be somewhat consistent with our ISCCP observational results in terms of the spatial pattern and sign, though the sensitivity of the modeled low clouds to ω_{700} is considerably enhanced. The modeled low cloud relationship to sea-surface temperature is generally consistent with the ISCCP observational results. The modeled low clouds are more dependent on temperature advection and wind speed in piControl than in the historical output, yet the magnitudes of the T_{adv} and WS relationships in piControl are more comparable to the observational results than they are in the historical output.

The differences in low cloud sensitivities to cloud controlling factors among the two ensembles are somewhat, though not entirely, surprising given the differences in the way the ISCCP simulator defines low clouds and the way we define them in the historical simulations. Determining the sign and magnitude of the spread in the sensitivities in LCF to CCFs is complicated by these differences, though we have been able to draw the following conclusion: modeled Sc and ShCu are too sensitive to EIS, SST, RH and ω_{700} compared with observations. Additionally, EIS is the

strongest control on low clouds in both ensembles, though the historical ensemble suggests LCF sensitivities to SST, RH, and ω can exceed that of EIS in certain regions.

Assessing the standard deviation of the regression coefficients, we see that there is the largest spread in the responses of the low clouds to EIS, SST, and T_{adv} in the Sc regions, though the largest spread in any quantity is occurring near the equator (Figures 24 and 26). This is also where the largest change in low clouds occurs in the ensembles (Figure 23 and 25), though the change is notably larger along the equator in the piControl ensemble than in the historical. We, again, speculate that these differences may have to do with the differences in low cloud fraction definitions in historical vs. piControl. In piControl, we attribute the larger decrease in cloud fraction along the equator (Figure 25) to the enhanced decrease in low cloudiness contributed by the ω changes (Figure 20), as a decrease in subsidence decreases LCF in this ensemble, and the change in ω is such that subsidence is reduced along the equator in response to interannual warming (driven largely by El Niño events). On the other hand, in the historical ensemble, the response of LCF to ω changes is the opposite: subsidence reduction increases low clouds. This response reduces the modeled LCF reduction in the historical ensemble that occurs as a result of EIS decreases and SST increases (Figure 23).

Connections between temperature and cloudiness mediated by meteorology

If we examine changes in low cloudiness in response to interannual warming through each individual cloud controlling factor in greater detail, we see relationships borne out which seem to be more in-line with the observed relationships than either of their constituent parts are. Except for EIS, which is more similar to just ERA-5 based results, the five other CCFs are quite in tune with their observed equivalents, shown in Figures 19 and 20. Relative humidity at 700 hPa translates increases along into increases in low cloudiness while decreases in downward motion at the same level are translated into either increases in cloudiness (historical) or decreases in cloudiness

(piControl). Broad increases in SST in response to warming decrease cloudiness in many regions, with slight increases in response to relative cooling in some ShCu regions. Changes in response to changing T_{adv} and WS are quite minimal, owing to the small sensitivity of LCF to these quantities and the small change in these quantities in response to surface warming. A broad region encompassing $\sim 10^\circ$ of latitude about the ITCZ in either direction which stretches across the whole of the Pacific where EIS increases though clouds only increase (summing across all CCF contributions) in the SH. This is likely because in this region of the SH, low clouds increase in response to increasing SSTs also (most probably ShCu) while they decrease in response to SSTs in the NH (in the region of EIS increase in the northeast Pacific). The canceling effects of the SST sensitivity (and the dominance of the SST sensitivity; Figures 31 and 33) drive the decrease in LCF in the NH while LCF increases in the SH are a combined effect of SST and EIS (relationships summarized in Figure 35).

In summary, in the historical simulations, a decrease in EIS along the equator is the key driving factor reducing low cloudiness there, with increases in SST driving the decrease in low clouds slightly north and south of the equator. Decreases in EIS drive decreases in low clouds in the subtropical Pacific Sc regions. For instance, in the SE Pacific Sc zone, a mix of SST and EIS changes act to reduce Sc. RH appears to be the primary driver of LCF changes in Sc-ShCu transition regions and along deep convective margin regions (for instance, decreases in RH increase low clouds in the Maritime Continent and west Pacific warm pool region) and ω_{700} dominates the LCF response in ascent regions in response to large-scale changes to the tropical overturning circulation. The summary of these relationships is also largely similar for the piControl models, though there is generally a stronger control of SST and smaller control of RH_{700} on LCF changes.

Summing the individual cloud responses to warming through CCFs as a reconstruction of cloud response to warming, and comparing that to the response directly calculated by regressing

LCF onto global mean surface temperatures suggest that the six chosen CCFs are fairly representative of the whole relationship. Unlike for the observations, the magnitudes of the changes shown for the reconstructed vs. direct LCF change are quite similar to one another. This suggests that nonlinearities or missing variables are not critical to the prediction of LCF changes in the models, whereas they may be in the observations.

C. Discussion

In a recent study (Myers et al. 2021), the authors found similar results to those presented here regarding the sensitivities of cloudiness to a selection of CCFs. However, there are two important differences between this work and theirs: (1) they do not examine the change in low cloudiness directly, but rather the change in low cloud induced radiative flux R , and (2) they only show changes in R on a domain-averaged basis, not how the relationships vary spatially. They also found that the response of R to EIS and SST in models is stronger than in the observations for both Sc and ShCu regimes, as is the modeled sensitivity of dR/dRH_{700} for trade cumulus (their Figures S8 and S9). They also found that dR/dT_{adv} is reduced, in alignment with the findings presented here, though they did not find a stronger sensitivity of R to vertical motion in the models than in the observations, nor did they find that dR/dWS is smaller for the models than the observations, as I have in this analysis. Possible reasons for these discrepancies are (a) different model ensemble members defining the bounds of the spread, (b) different definitions of ShCu and Sc regions, especially when much of the sensitivity is expressed along the equator in the EPac, which does not clearly fall within either their Sc or ShCu definitions, and (c) using R instead of LCF.

D. Conclusion

Here, I examine the relationships between LCF and CCFs and CCFs to surface temperature changes to compare with our observational results to assess potential drivers of spread in the low cloud feedback among GCMs. I employ two model ensembles: an ensemble (2000-2014) that

includes aerosol and greenhouse gas forcings from the historical period, and one that only includes pre-industrial forcings.

Across both model ensembles, I find that models characterize low clouds as being much more sensitive to every CCF, except wind speed and temperature advection, than the observations do. This represents a primary difference between observations and GCMs in representing cloud changes in cloud-climate feedbacks. Generally, piControl clouds are more sensitive to meteorology; this is especially evident in EIS and SST, with for example the average response of piControl low cloudiness to EIS being $\sim 7\% \sigma^{-1}$ greater in Sc regions than its historical counterpart (Figure 23 and 25). Where the divergence is most stark in the relationship between cloudiness and vertical motion: for the historical ensemble, there exists a relationship wherein heightened subsidence decreases cloudiness (Figure 23 and 25). In the piControl ensemble, this relationship is inverted, with increased subsidence increasing cloudiness. This, then, suggests that the relationship with vertical motion, in particular, is highly dependent on the definition of low cloudiness, even despite controlling for overlap issues between high and low clouds present within the ISCCP simulator output that might erroneously emphasize a sensitivity to vertical motion within the analysis (as high clouds are closely tied to vertical motion in the tropics). Different methods are used to define cloudiness in the two ensembles. In the historical models, the maximum cloudiness between 1000-600 mb assuming maximum overlap is used as the LCF definition. In the piControl models, the cloudiness product is a satellite simulator — in particular, it simulates what the satellites would directly sense. This leads to nontrivial differences in the low cloud climatology, whereby the historical ensemble LCF definition appears to contain more trade cumulus and mid-level clouds than the piControl ensemble (an example of which is shown in Figure 36) and likely contributes to the differences shown among the ensembles in $dLCF/dCCF$.

Next, I find that there is not one spatially uniform primary contributor of uncertainty to models in cloudiness-warming relationships. In Figures 24 and 26, we see that the spread in $dLCF/dCCF$ is largest in the SE Pacific stratocumulus regions and along the equator for both model ensembles. The spread is largest for SST and EIS in piControl and EIS and RH in the historical ensemble; these differences are likely attributable to the different LCF definitions. The spread in $dCCF/dT_s$, however, is largest along the equator in both ensembles (Figures 21 and 22). In other words, the spread in $dLCF/dT_s$ in the heart of Sc regions (at least in the SE Pacific) is coming from the spread in $dLCF/dCCF$ while the spread in $dLCF/dT_s$ along the equator is coming from the model spread in the different responses of CCFs to T_s . In piControl, the spread in $dEIS/dT_s$ is much smaller than in the historical ensemble, and the spread in dT_{adv}/dT_s is much larger. The spread in the other quantities is similar for both ensembles, most probably due to the fact that the response of CCFs to warming is similar for the other variables. The only major difference in the response of CCFs to warming among the piControl and historical ensembles is that the response of EIS to interannual warming is depressed in piControl models in comparison to the historical models.

The largest mean changes and largest contributions to spread in cloud-warming relationships (in both ensembles) in the tropics occur in the equatorial Pacific and arise due to the EIS, SST, and ω_{700} components of the low cloudiness-warming reconstructions (Figures 27-30). Relative humidity also is an active contributor, but only in the west Pacific, and only in the historical ensemble. Therefore, we caution that the larger contribution from RH_{700} and ω_{700} in both model ensembles than in the observations suggests that models are too sensitive to changes in the large-scale overturning circulations (the Hadley and Walker cells, in the tropics). These results highlight priorities for improving parameterization of low cloud processes.

IV. Figures

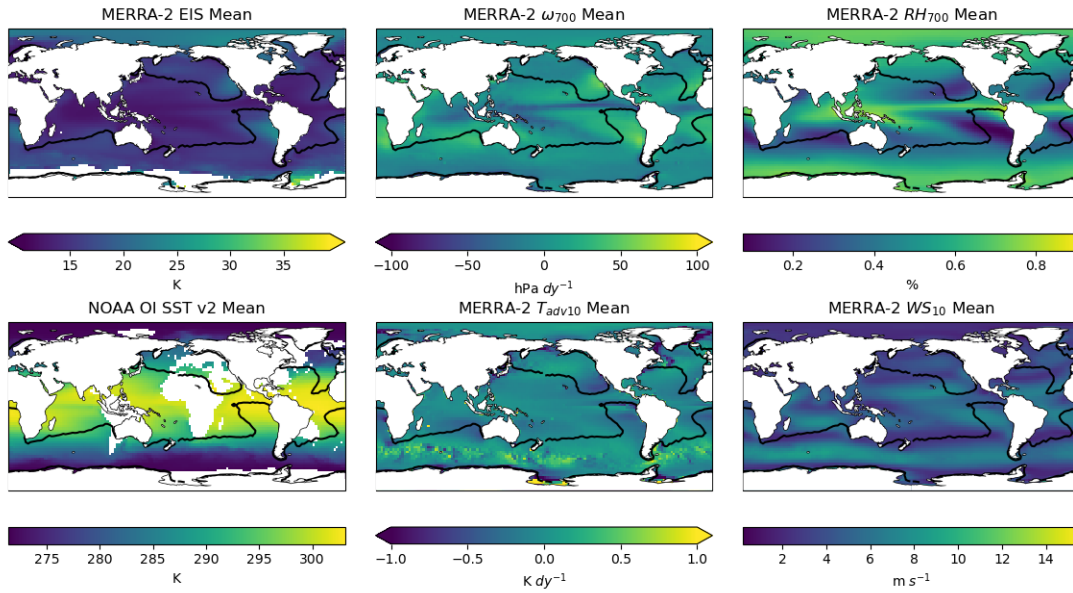


Figure 1: 1997-2015 climatologies of MERRA-2 cloud controlling factors (EIS, ω_{700} , RH_{700} , T_{adv} , and WS) and NOAA OI SSTs. Clockwise, from top left: EIS, ω_{700} , RH_{700} , WS, T_{adv} , SST.

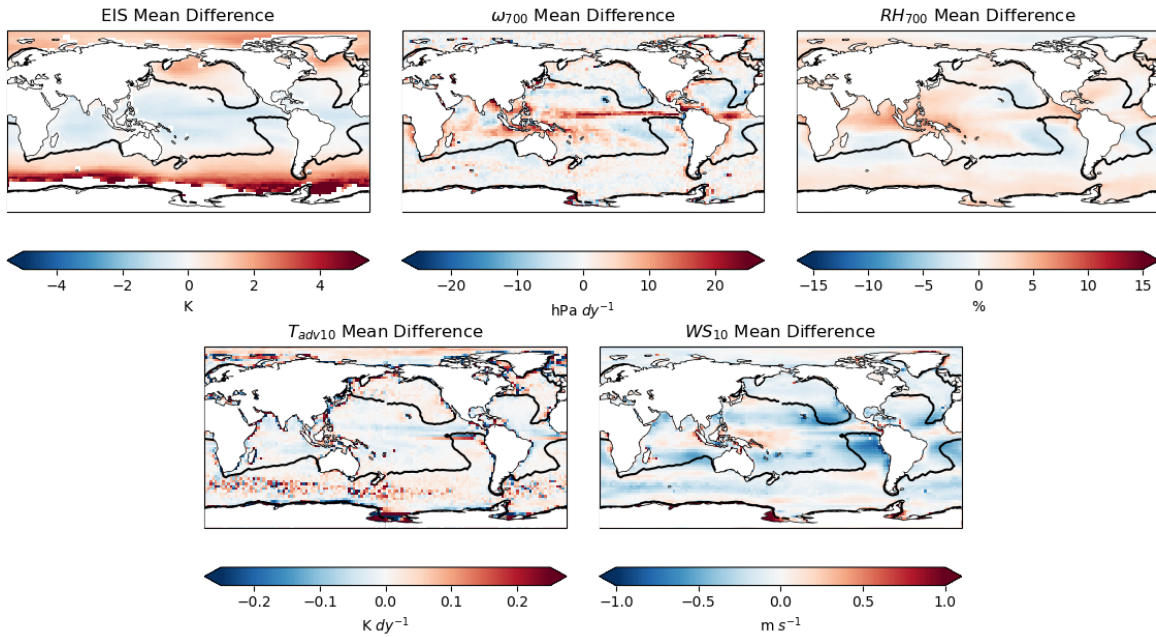


Figure 2: Difference in mean meteorological cloud controlling factors from MERRA-2 and ERA-5.

ERA-5 subtracted from MERRA-2. Clockwise, from top left: EIS , ω_{700} , RH_{700} , WS_{10} , T_{adv10} .

Mean state of cloudiness for CASCAD boundary layer clouds and ISCCP total LCF

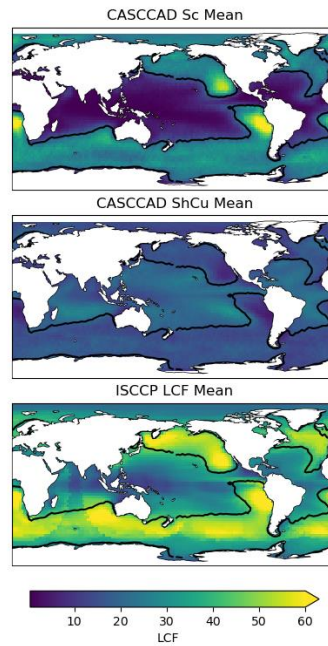


Figure 3: 2007-2015 climatologies of CASCAD Sc (top) and ShCu (middle) cloudiness; 1997-2008 climatology of ISCCP LCF (bottom) cloudiness.

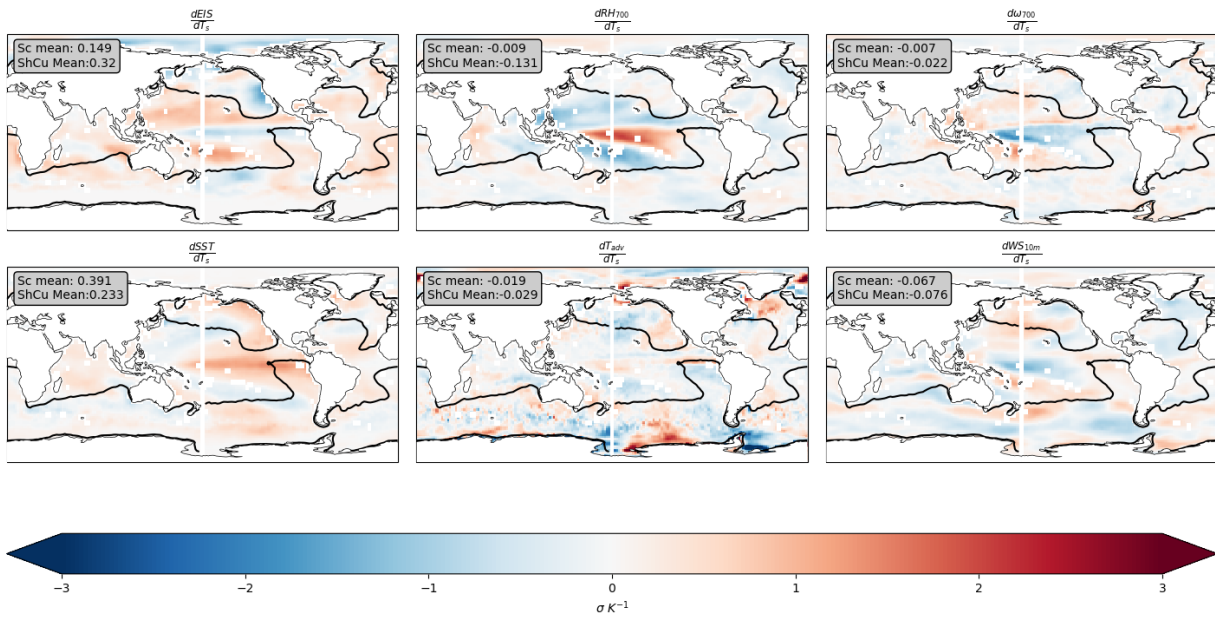


Figure 4: Linear regression coefficients for each CCF regressed onto NOAA OI global mean surface

temperature at each gridpoint in MERRA-2 for 2007-2015. Clockwise, from top left: EIS, ω_{700} ,

RH₇₀₀, WS₁₀, T_{adv10}, SST.

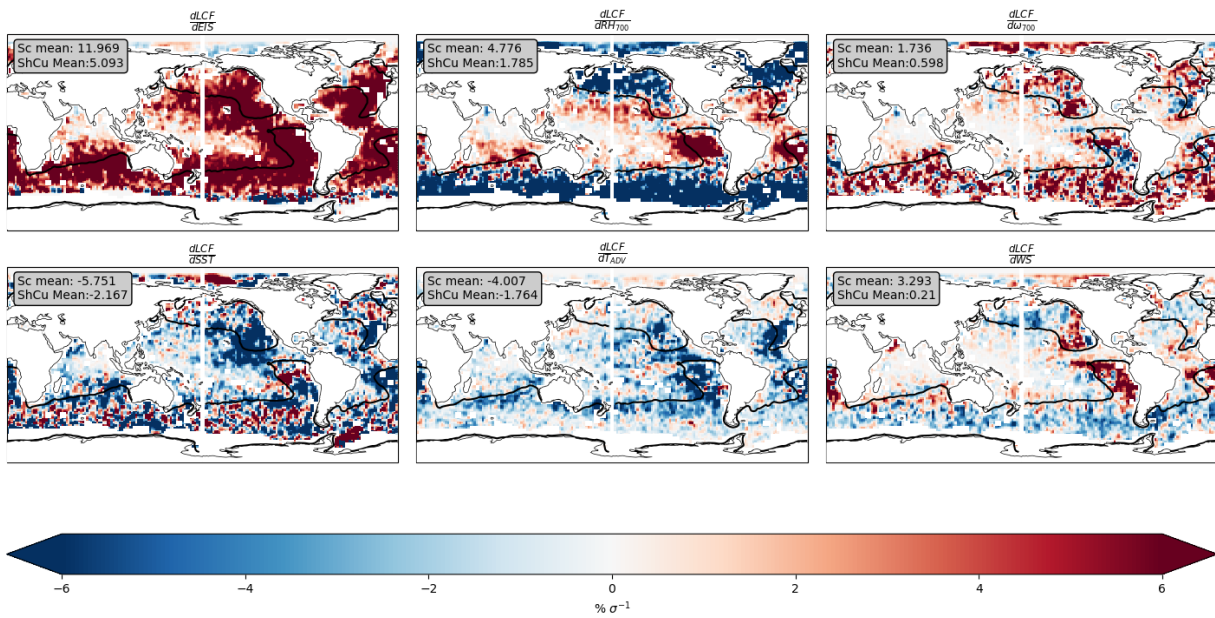


Figure 5: Multiple linear regression coefficients for CASCCAD Sc cloudiness regressed onto each MERRA-2 CCF and NOAA OI SST at each gridpoint. Clockwise, from top left: EIS, ω_{700} , RH₇₀₀,

WS₁₀, T_{adv10}, SST.

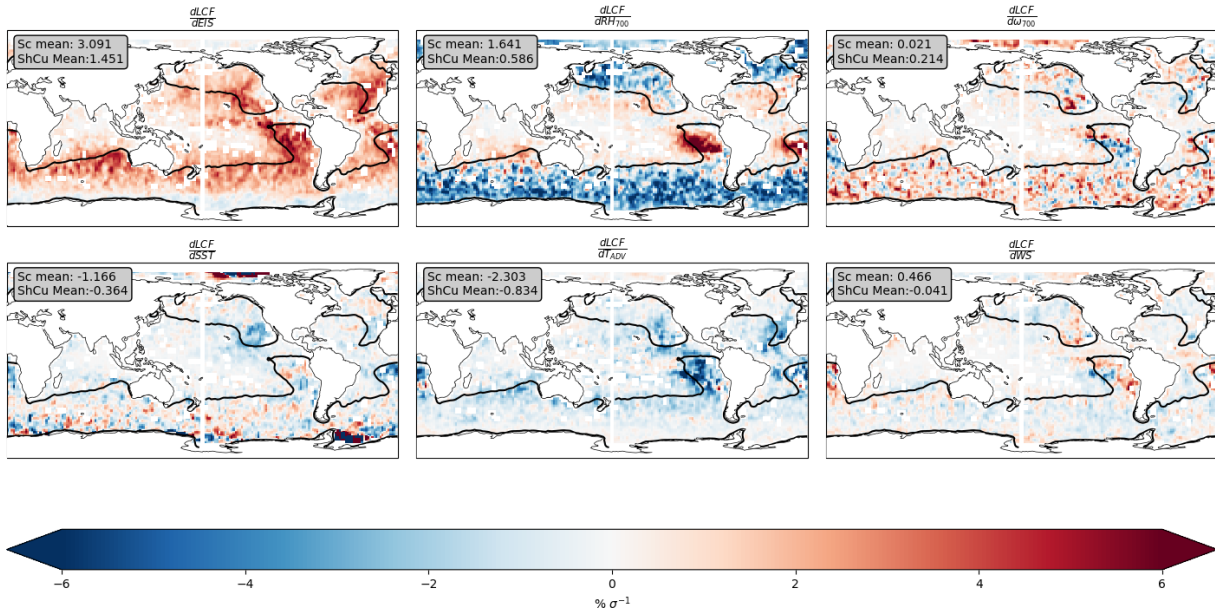


Figure 6: Multiple linear regression coefficients for CASCCAD Sc cloudiness regressed onto each ERA-5 CCF and NOAA OI SSTs at each gridpoint. Clockwise, from top left: EIS, ω_{700} , RH₇₀₀,

WS₁₀, T_{adv10}, SST.

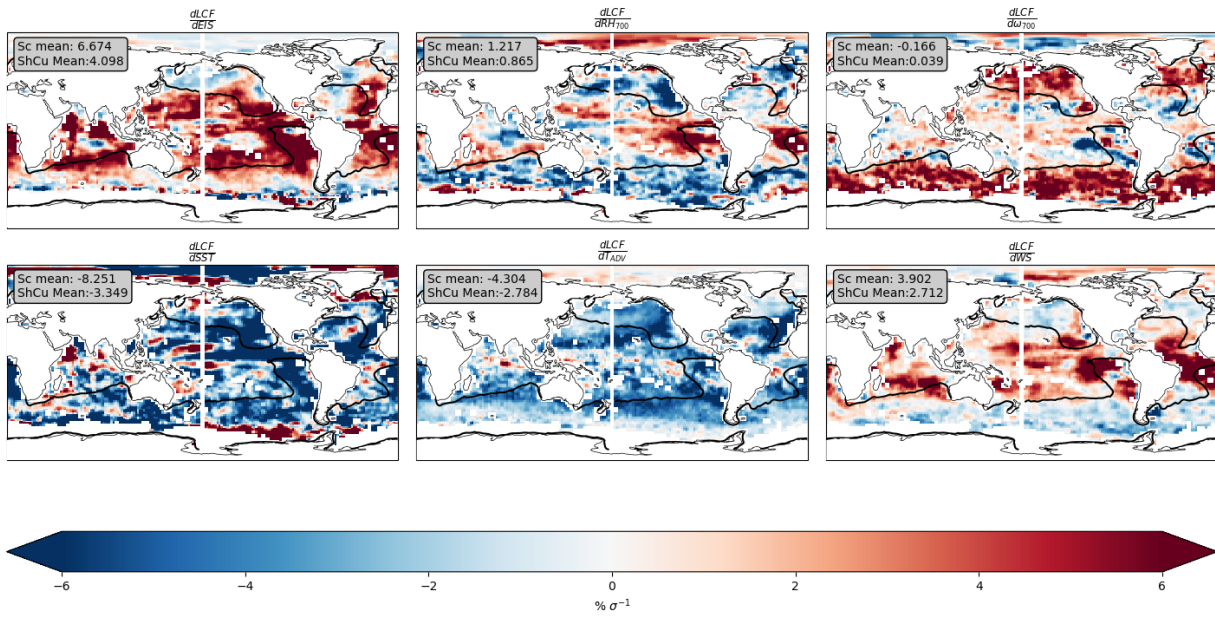


Figure 7: Multiple linear regression coefficients for ISCCP low cloudiness regressed onto each MERRA-2 CCF and NOAA OI SSTs. Clockwise, from top left: EIS, ω_{700} , RH₇₀₀, WS₁₀, T_{adv10}, SST.

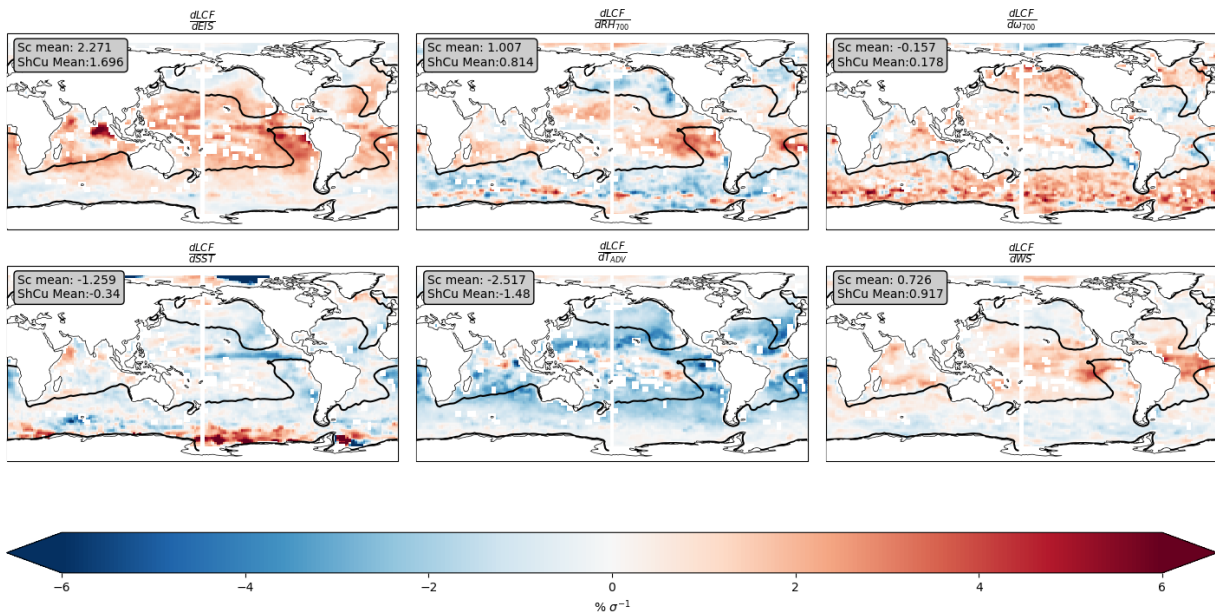


Figure 8: Multiple linear regression coefficients for ISCCP low cloudiness regressed onto each ERA-5 CCF and NOAA OI SSTs. Clockwise, from top left: EIS, ω_{700} , RH₇₀₀, WS₁₀, T_{adv10}, SST.

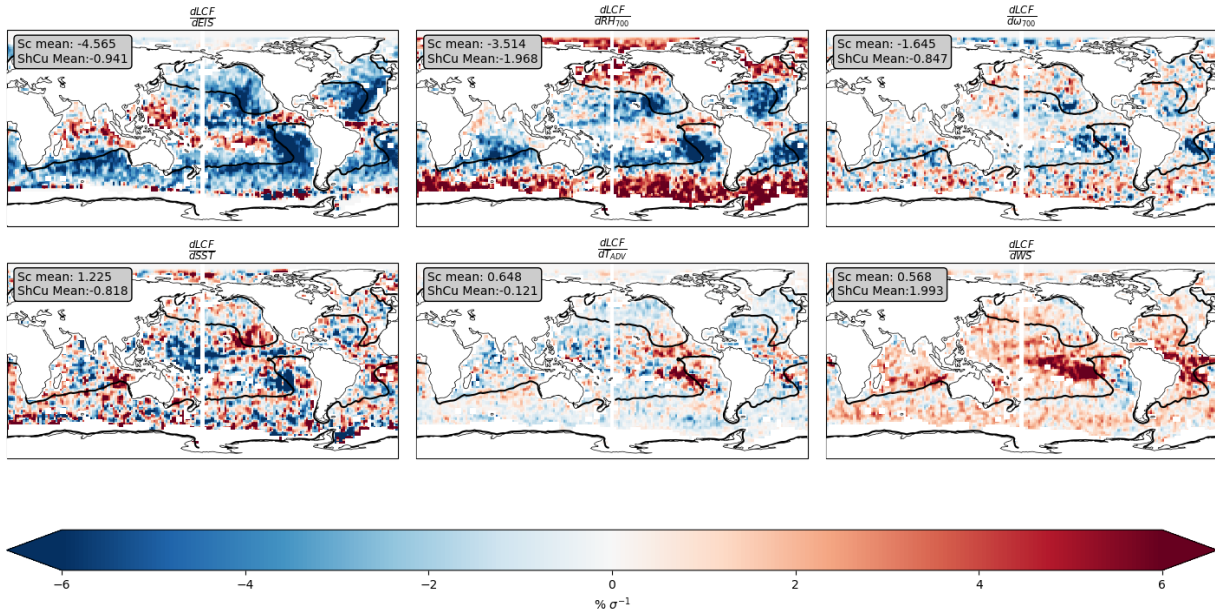


Figure 9: Multiple linear regression coefficients for CASCCAD ShCu cloudiness regressed onto each MERRA-2 CCF and NOAA OI SSTs. Clockwise, from top left: EIS, ω_{700} , RH₇₀₀, WS₁₀, T_{adv10}, SST.

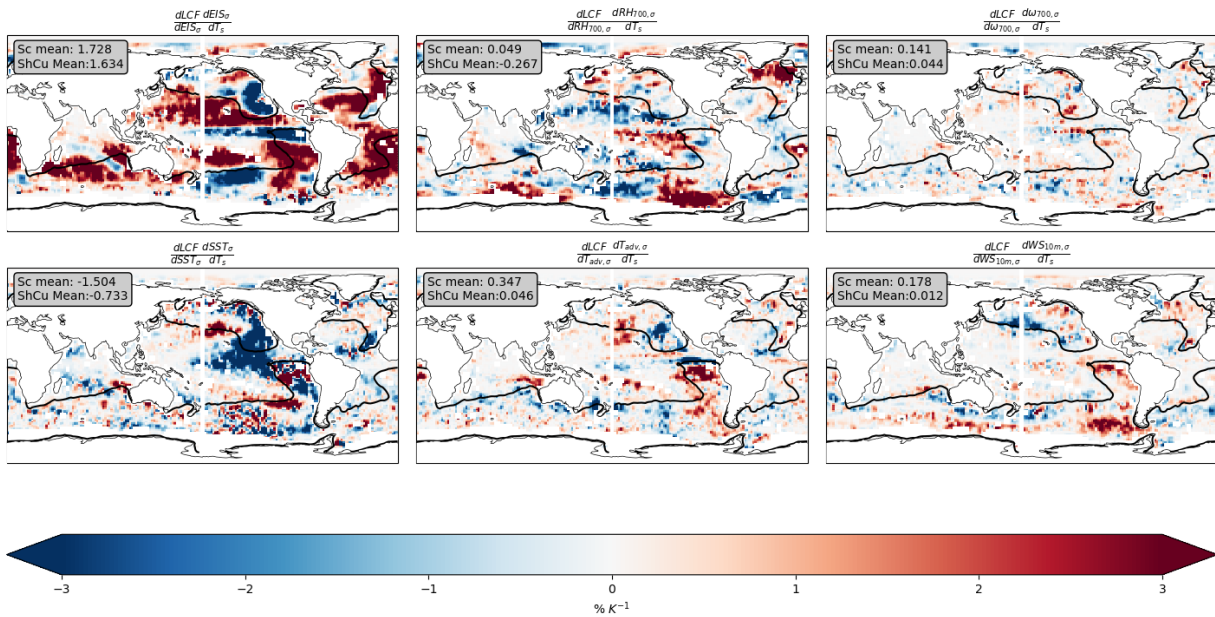


Figure 10: Products of CASCCAD Sc cloudiness regressed onto each MERRA-2 CCF with MERRA-2 CCF and NOAA OI SST single regressions onto NOAA OI global mean surface temperature. Clockwise, from top left: EIS, ω_{700} , RH₇₀₀, WS₁₀, T_{adv10}, SST.

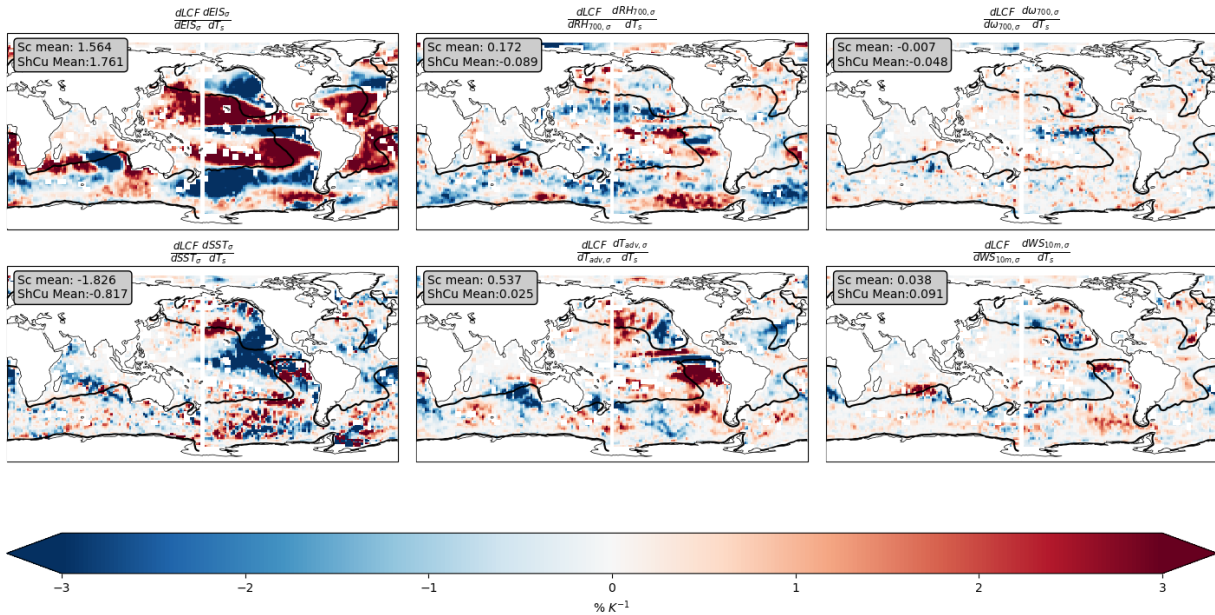


Figure 11: Products of CASCCAD Sc cloudiness regressed onto each ERA-5 CCF with ERA-5 CCF and NOAA OI SST single regressions onto NOAA OI global mean surface temperature. Clockwise, from top left: EIS, ω_{700} , RH₇₀₀, WS₁₀, T_{adv10}, SST.

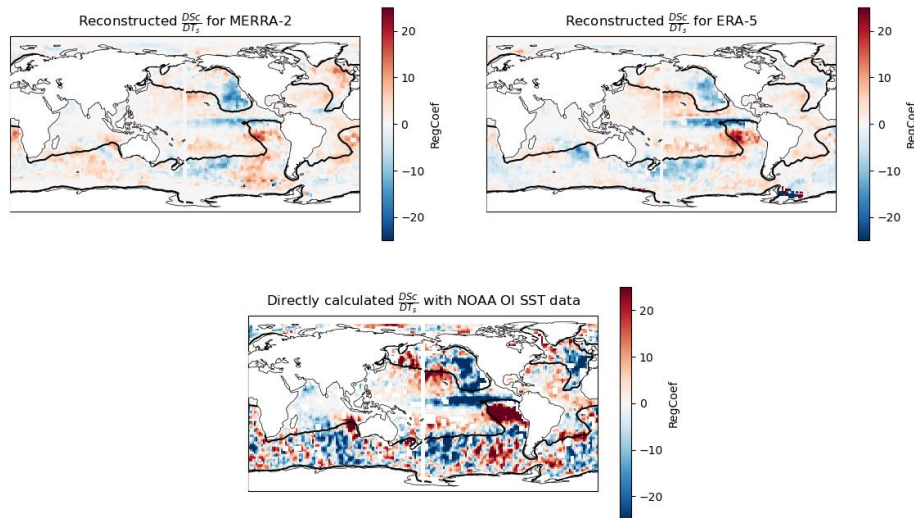


Figure 12: Comparison of directly regressed and reconstructed (as the sum of each term found in Figures 10 & 11) relationships between CASCCAD Sc cloudiness and reanalyzed global mean surface temperature. Left to right, top to bottom: reconstructed CASCCAD Sc cloudiness and NOAA OI global mean surface temperature relationships; reconstructed CASCCAD Sc cloudiness and NOAA OI global mean surface temperature; directly calculated CASCCAD Sc cloudiness and NOAA OI global mean surface temperature relationships

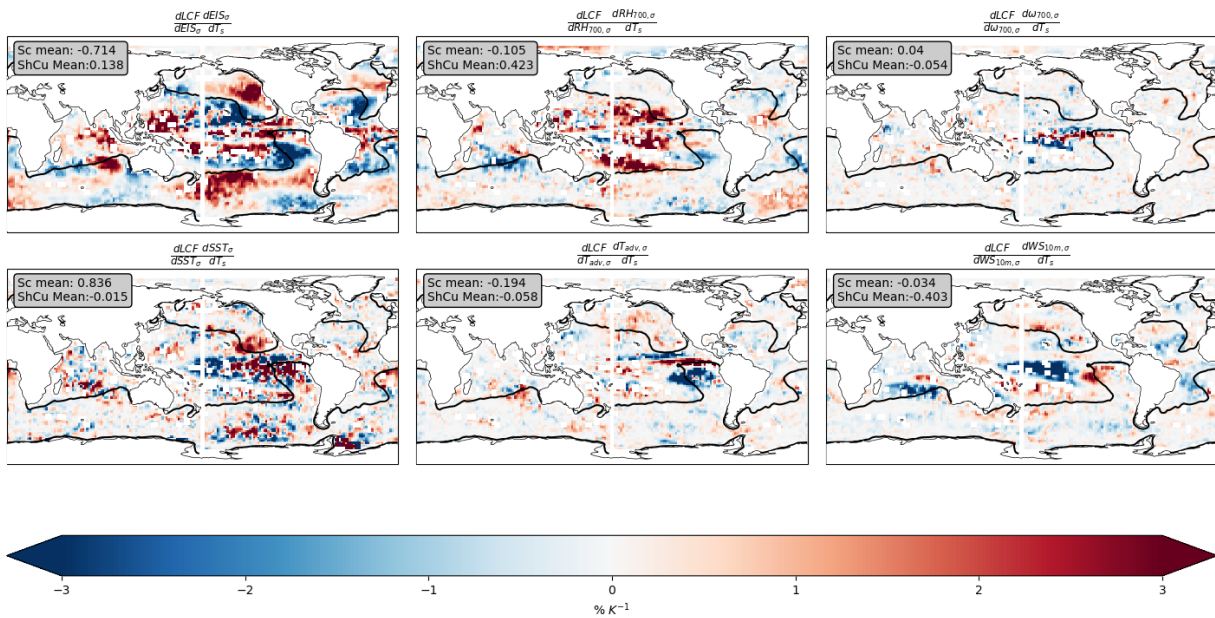


Figure 13: Products of CASCCAD ShCu cloudiness regressed onto each MERRA-2 CCF with MERRA-2 CCF and NOAA OI SST single regressions onto NOAA OI global mean surface temperature. Clockwise, from top left: EIS, ω_{700} , RH₇₀₀, WS₁₀, T_{adv10}, SST.

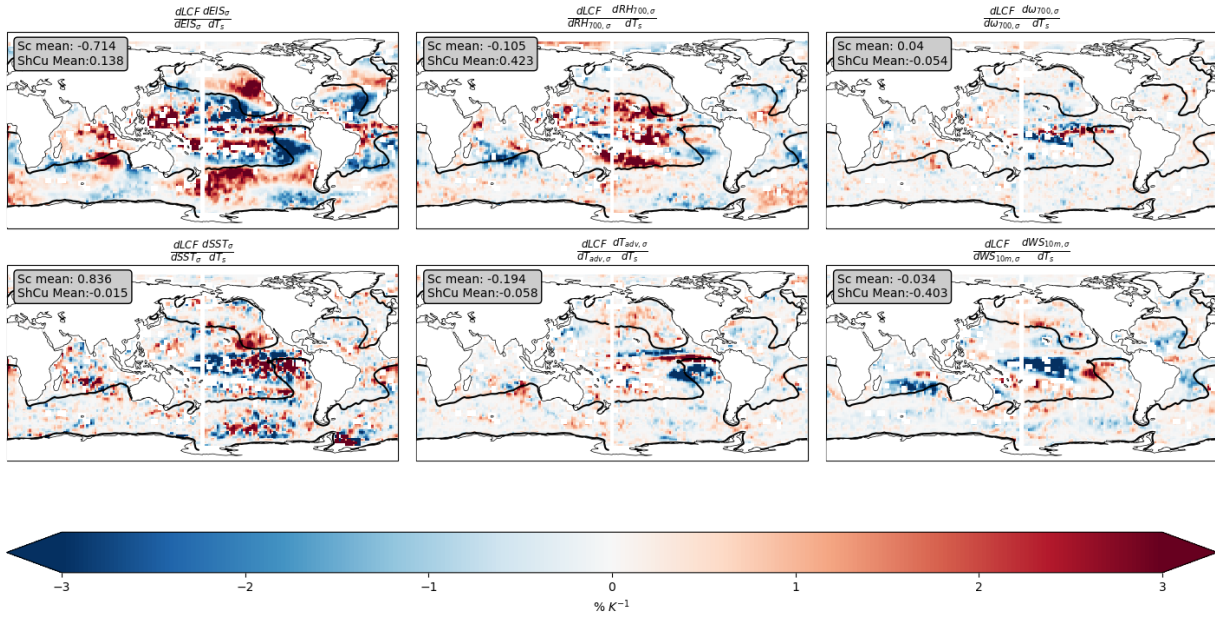


Figure 14: Products of CASCCAD ShCu cloudiness regressed onto each ERA-5 CCF with ERA-5 CCF and NOAA OI SST single regressions onto NOAA OI SST global mean surface temperature.

Clockwise, from top left: EIS, ω_{700} , RH₇₀₀, WS₁₀, T_{adv10}, SST.

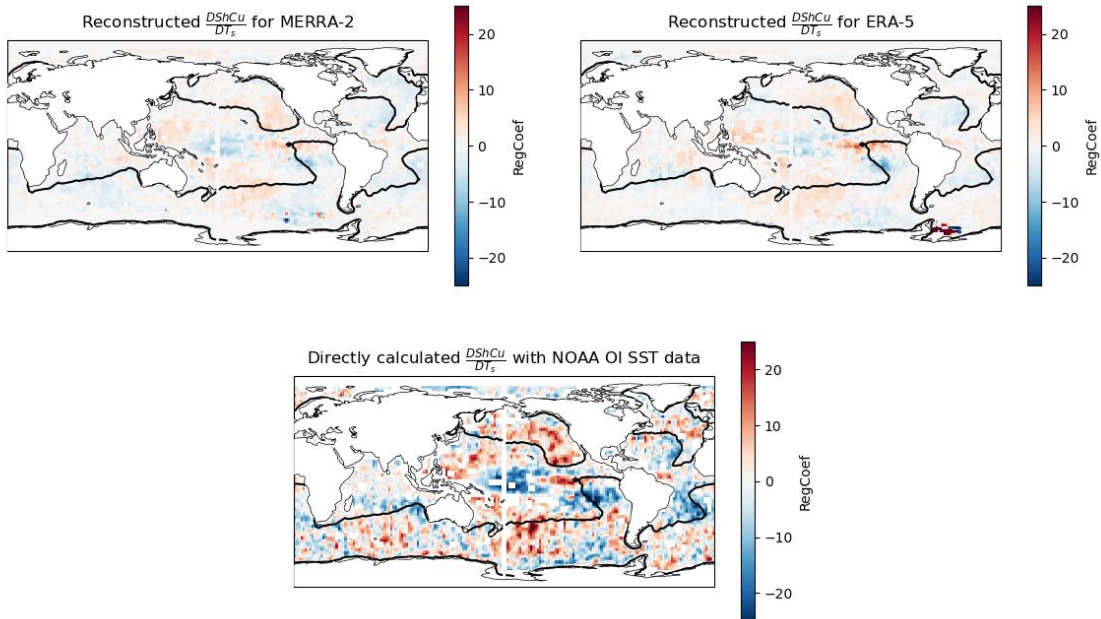


Figure 15: Comparison of directly regressed and reconstructed (as the sum of each term found in Figures 13 & 14) relationships between CASCCAD ShCu cloudiness and reanalyzed global mean surface temperature. Left to right, top to bottom: reconstructed CASCCAD ShCu cloudiness and NOAA OI global mean surface temperature relationships; reconstructed CASCCAD ShCu cloudiness and NOAA OI global mean surface temperature relationships; directly calculated CASCCAD ShCu cloudiness and NOAA OI global mean surface temperature relationships.

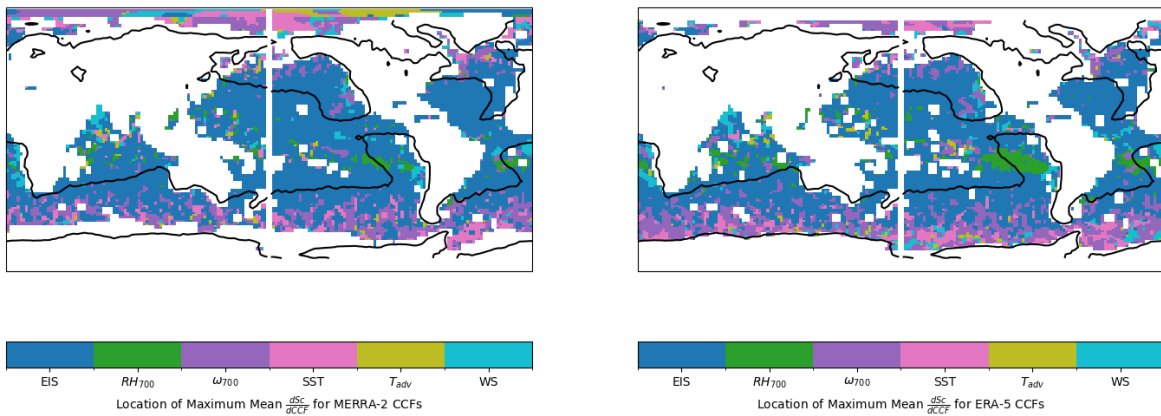


Figure 16: Maximum magnitude contributor to the multiple regression model of CASCCAD Sc cloudiness to MERRA-2 and ERA-5 CCFs at each grid point. Left: MERRA-2; right: ERA-5.

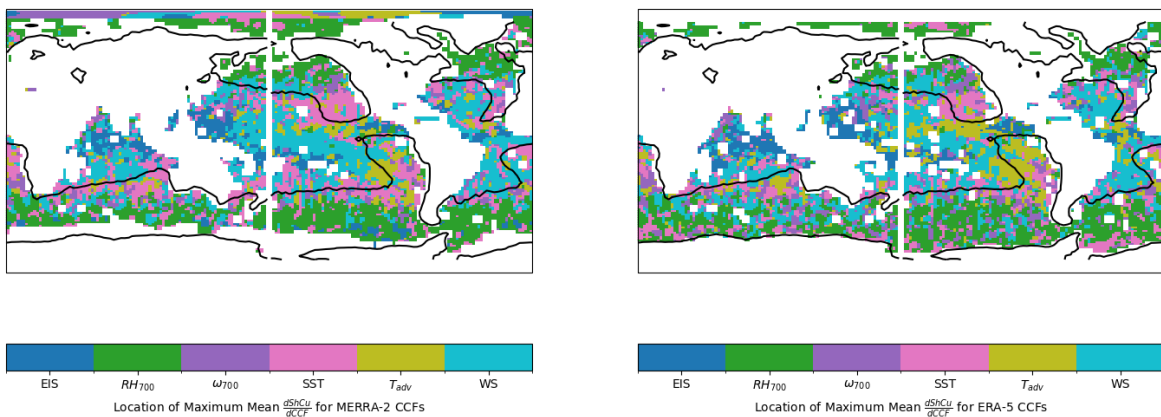


Figure 17: Maximum magnitude contributor to the multiple regression model of CASCCAD ShCu cloudiness to MERRA-2 and ERA-5 CCFs at each grid point. Left: MERRA-2; right: ERA-5.

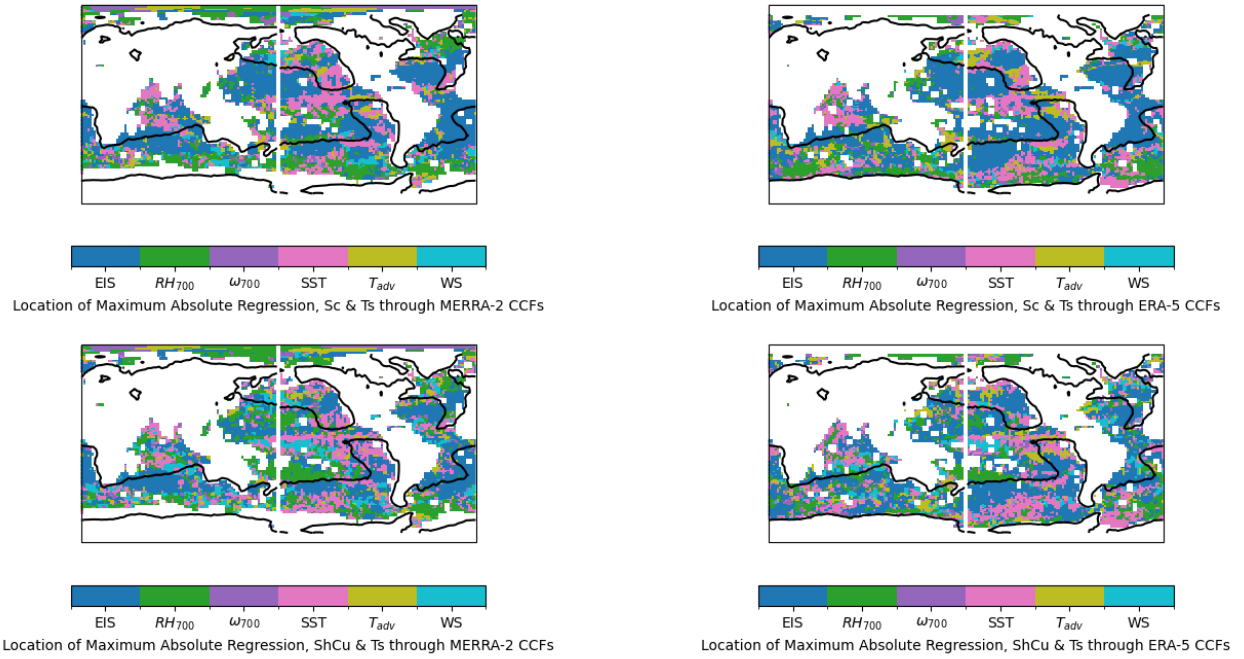


Figure 18: Maximum magnitude contributor to the reconstructed model of CASCCAD Sc and ShCu cloudiness to NOAA OI SST global mean surface temperatures at each grid point. Clockwise, from top left: CASCCAD Sc and MERRA-2 CCFs; CASCCAD Sc and ERA-5 CCFs; CASCCAD ShCu and ERA-5 CCFs; CASCCAD ShCu and MERRA-2

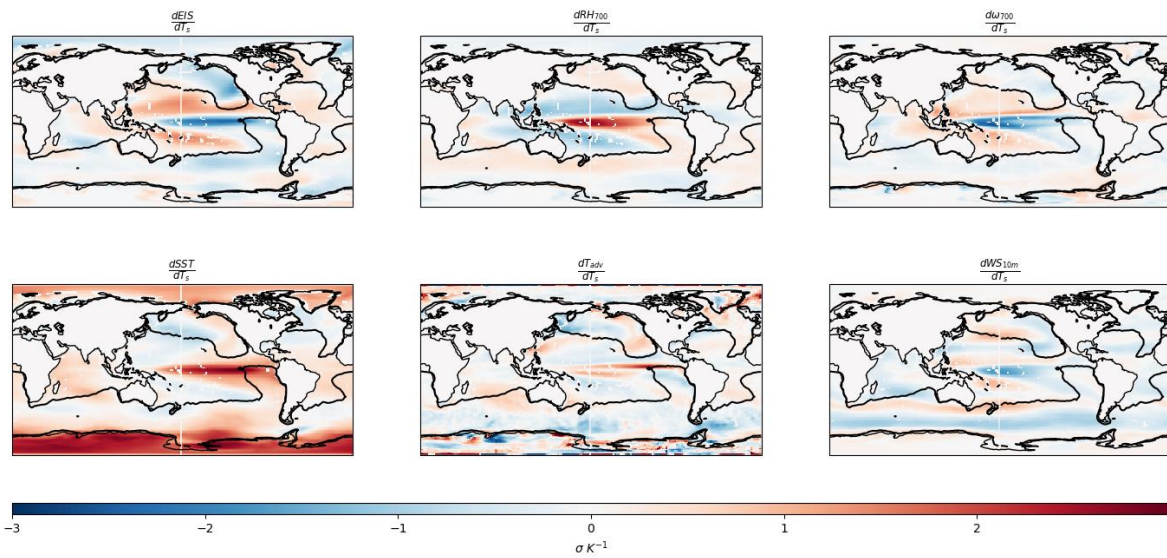


Figure 19: Mean historical model single linear response of each CCF to global mean sea surface temperatures. Clockwise, from top left: EIS; RH₇₀₀, ω_{700} , WS, T_{adv}, SST.

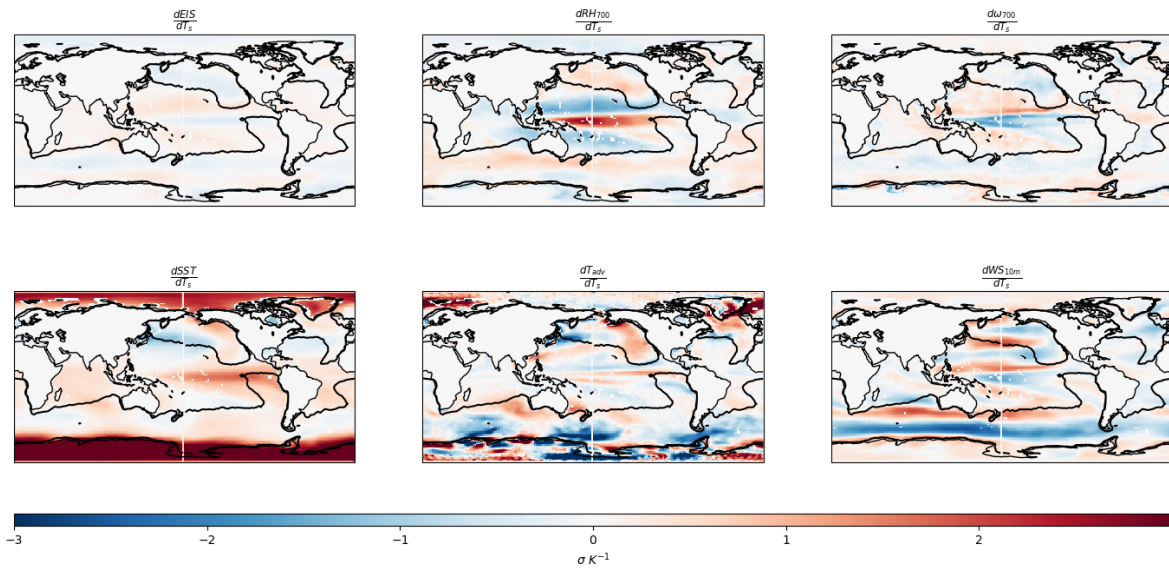


Figure 20: Mean piControl model single linear response of each CCF to global mean sea surface temperatures. Clockwise, from top left: EIS; RH₇₀₀, ω_{700} , WS, T_{adv}, SST.

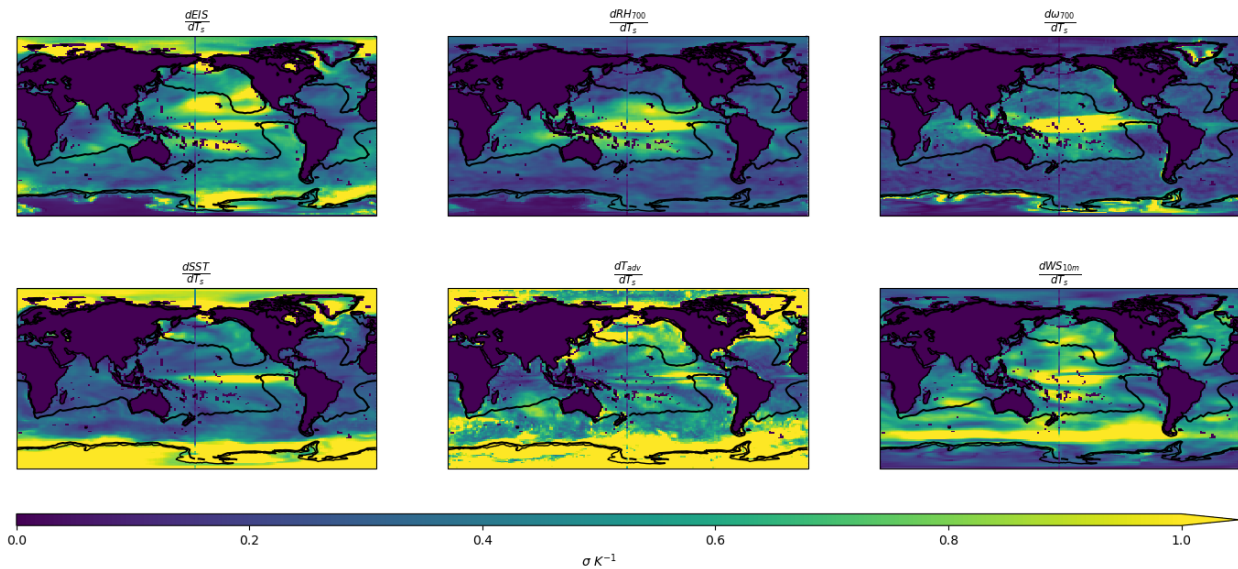


Figure 21: Cross-model standard deviation in historical modeled CCF-global mean surface temperature relationships. Higher values indicate more intermodel disagreement on representation of a characteristic. Clockwise, from top left: EIS; RH₇₀₀, ω_{700} , WS, T_{adv}, SST.

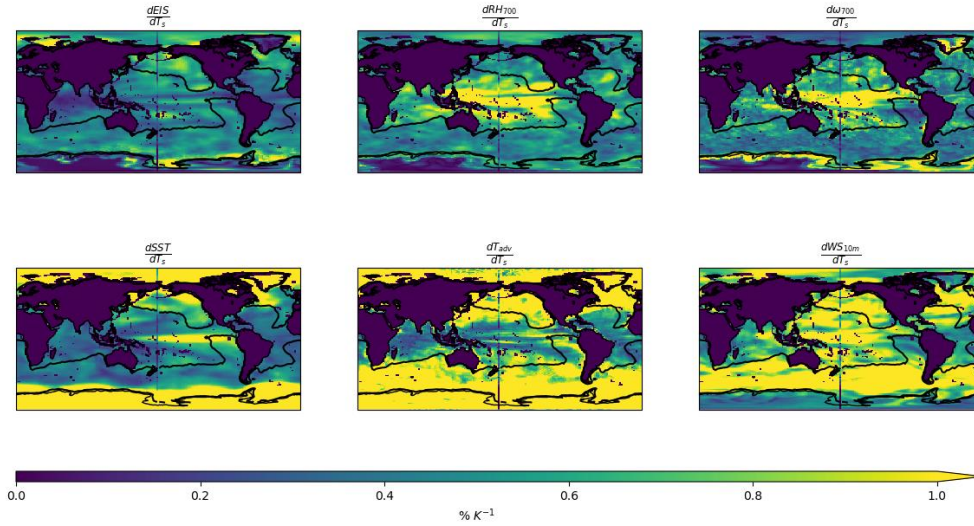


Figure 22: Cross-model standard deviation in piControl modeled CCF-global mean surface temperature relationships. Higher values indicate more intermodel disagreement on representation of a characteristic. Clockwise, from top left: EIS; RH_{700} , ω_{700} , WS, T_{adv} , SST.

Model average historic (200001-201412) response in LCF to CCFs standardized by ERA-5 observations.

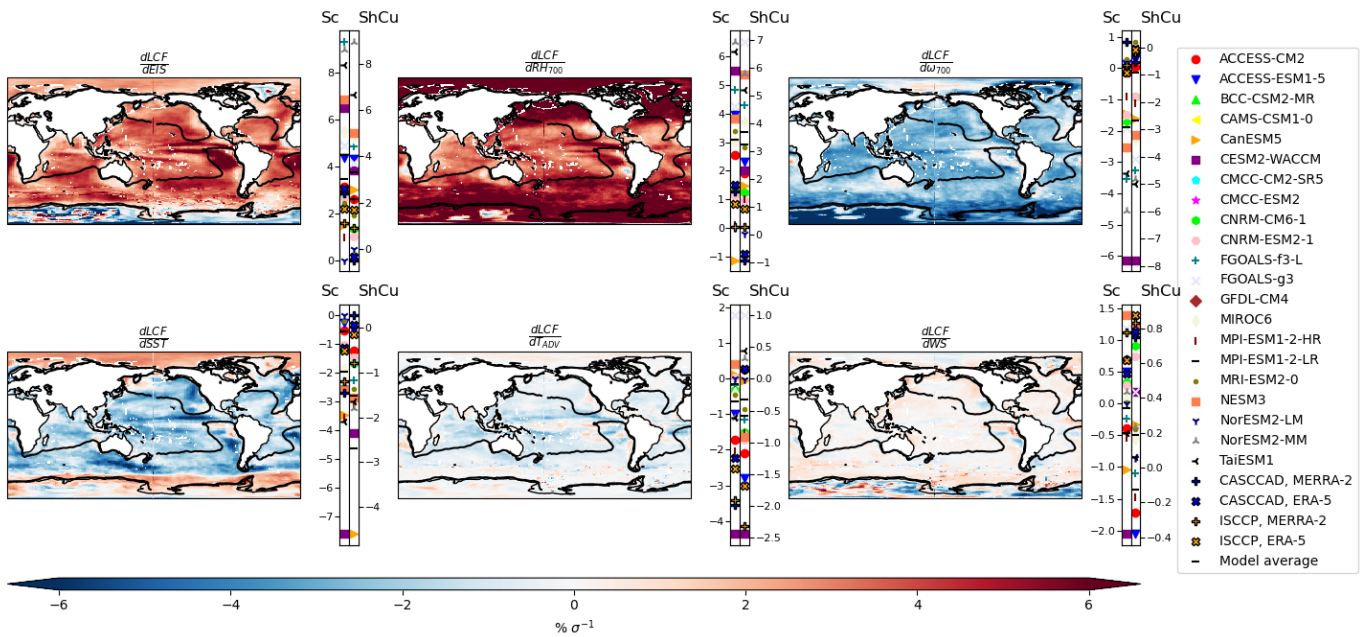


Figure 23: Historical model average multiple linear response in LCF to each CCF (maps) and individual model Sc- and ShCu-domain averaged response (scatterbars). Clockwise, from top left:

EIS; RH_{700} , ω_{700} , WS, T_{adv} , SST.

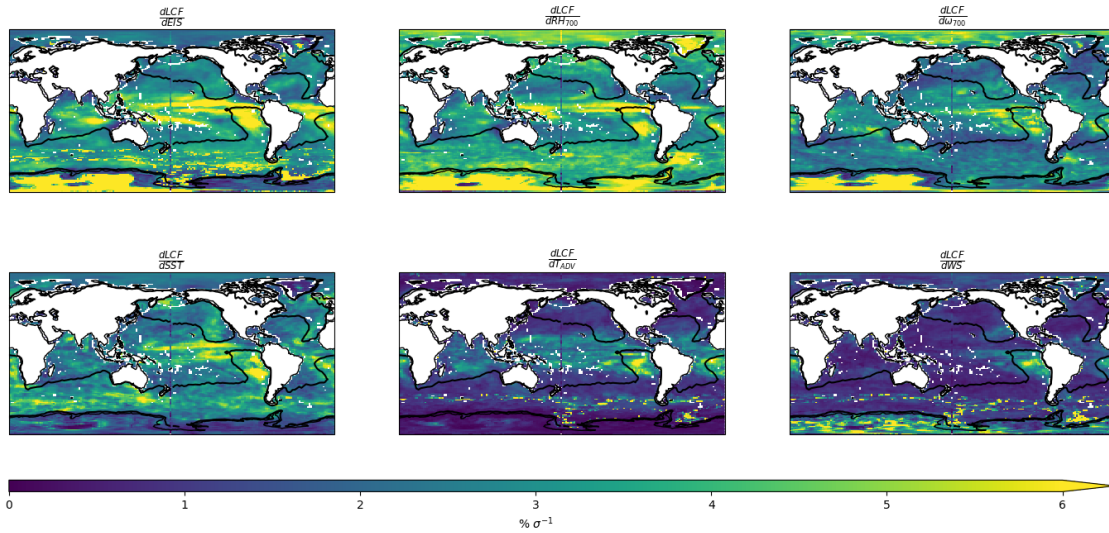


Figure 24: Cross-model standard deviation in historical modeled LCF-CCF relationships. Higher values indicate more intermodel disagreement on representation of a characteristic. Clockwise, from top left: EIS; RH₇₀₀, ω₇₀₀, WS, T_{adv}, SST.

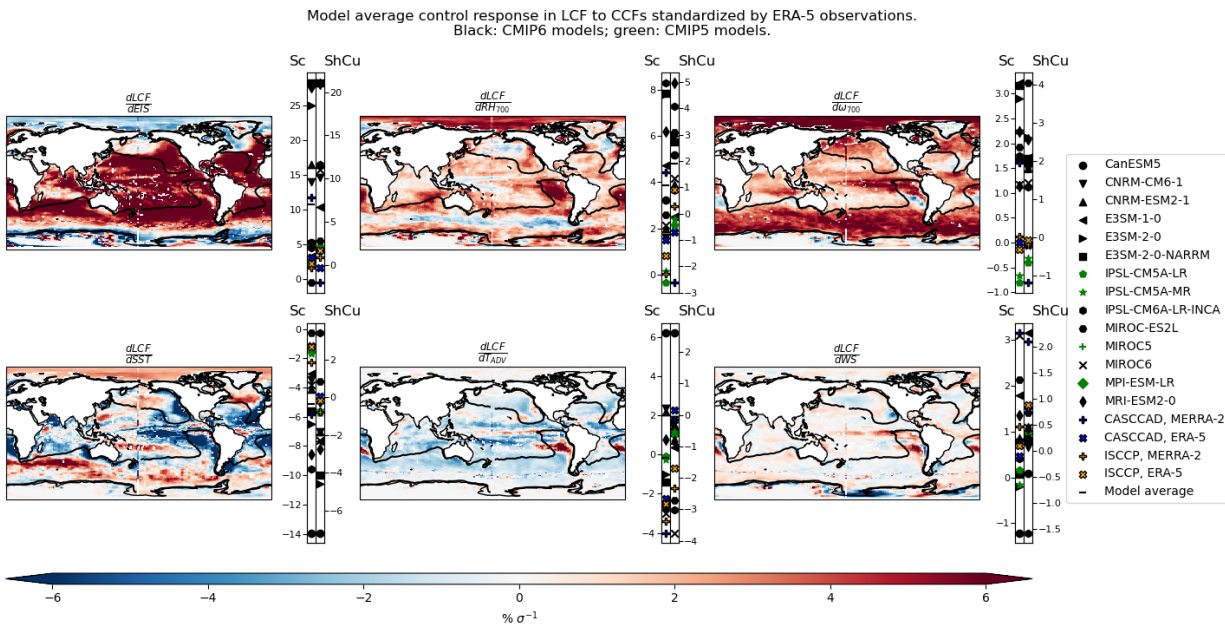


Figure 25: PiControl model average multiple linear response in LCF to each CCF (maps) and individual model Sc- and ShCu-domain averaged response (scatterbars). Clockwise, from top left:

EIS; RH₇₀₀, ω₇₀₀, WS, T_{adv}, SST.

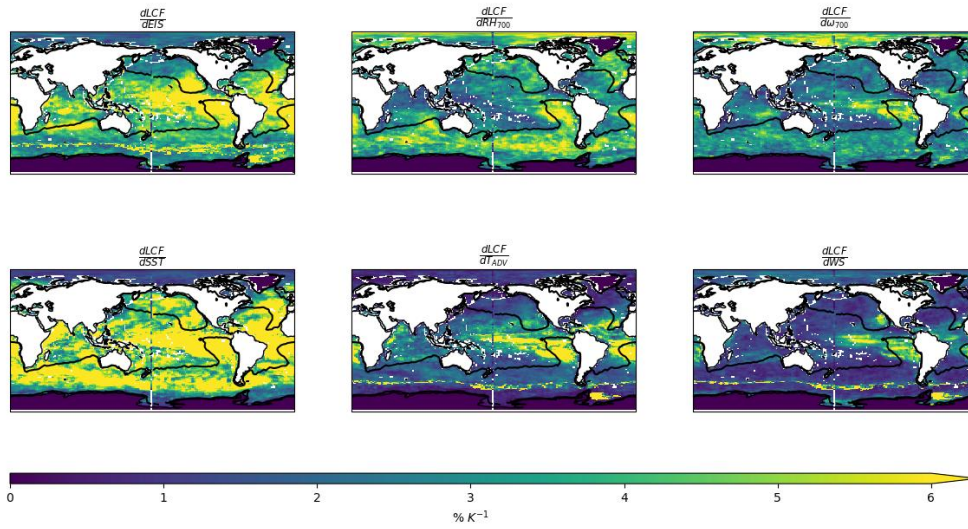


Figure 26: Cross-model standard deviation in piControl modeled LCF-CCF relationships. Higher values indicate more intermodel disagreement on representation of a characteristic. Clockwise, from top left: EIS; RH_{700} , ω_{700} , WS, T_{adv} , SST.

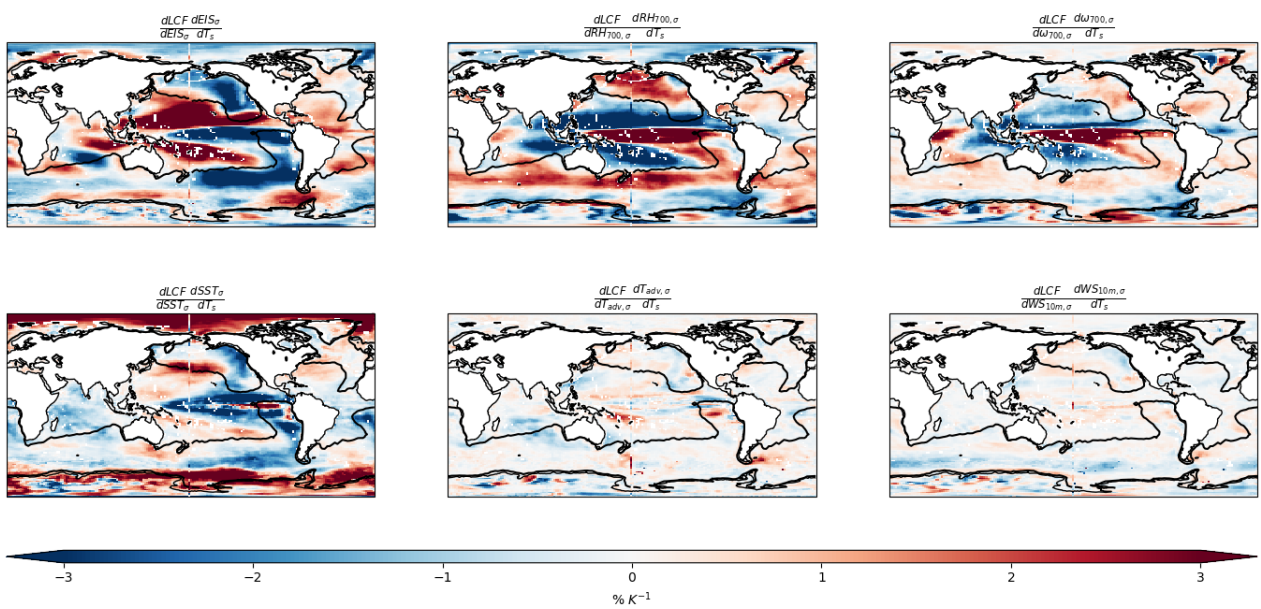


Figure 27: Products of historically modeled multiple linear LCF-CCF and single linear CCF- T_s relationships. Clockwise, from top left: EIS; RH_{700} , ω_{700} , WS, T_{adv} , SST.

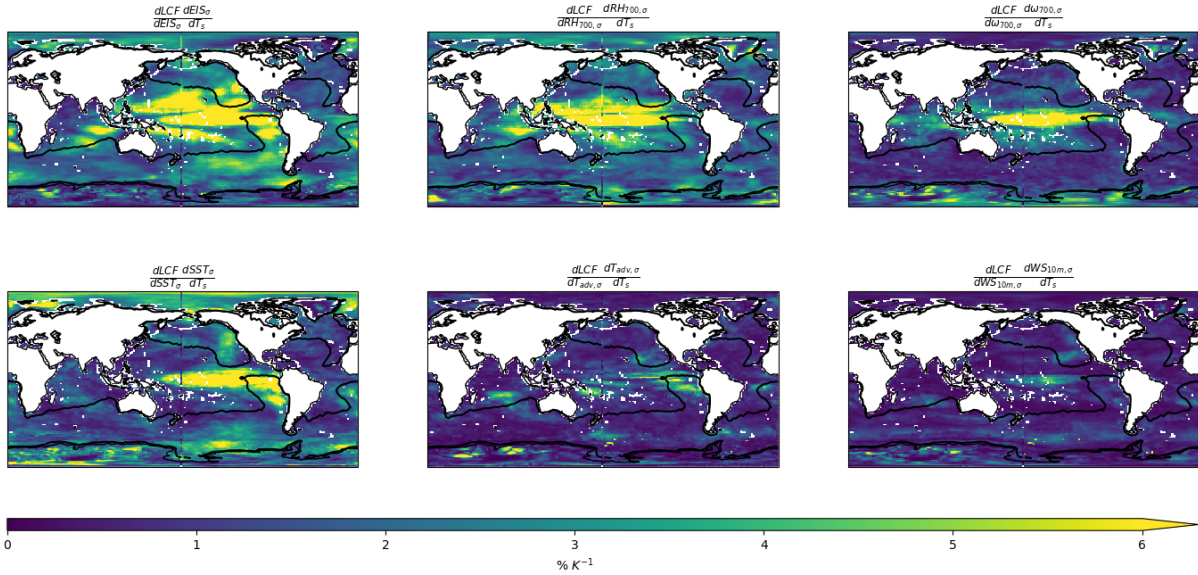


Figure 28: Cross-model standard deviation in historical modeled low cloudiness to global mean surface temperature through CCF relationships. Higher values indicate more intermodel disagreement on representation of a characteristic. Clockwise, from top left: EIS; RH_{700} , ω_{700} , WS, T_{adv} , SST.

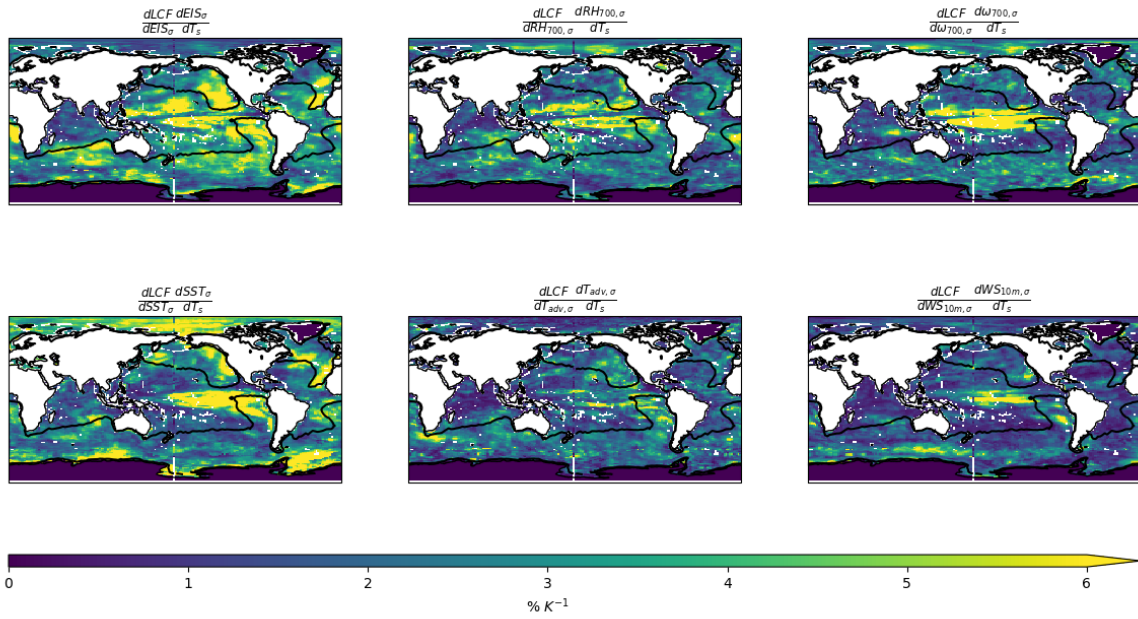


Figure 29: Cross-model standard deviation in piControl modeled low cloudiness to global mean surface temperature through CCF relationships. Higher values indicate more intermodel disagreement on representation of a characteristic. Clockwise, from top left: EIS; RH_{700} , ω_{700} , WS, T_{adv} , SST.

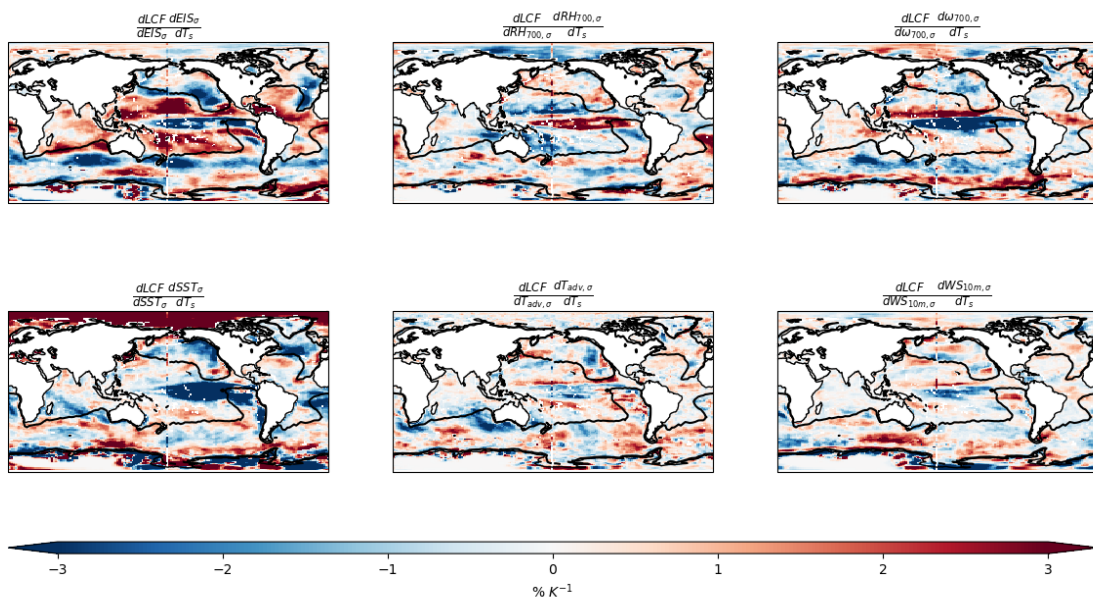


Figure 30: Mean piControl response of low cloudiness to sea-surface temperatures through each CCF. Clockwise, from top left: EIS; RH_{700} , ω_{700} , WS, T_{adv} , SST.

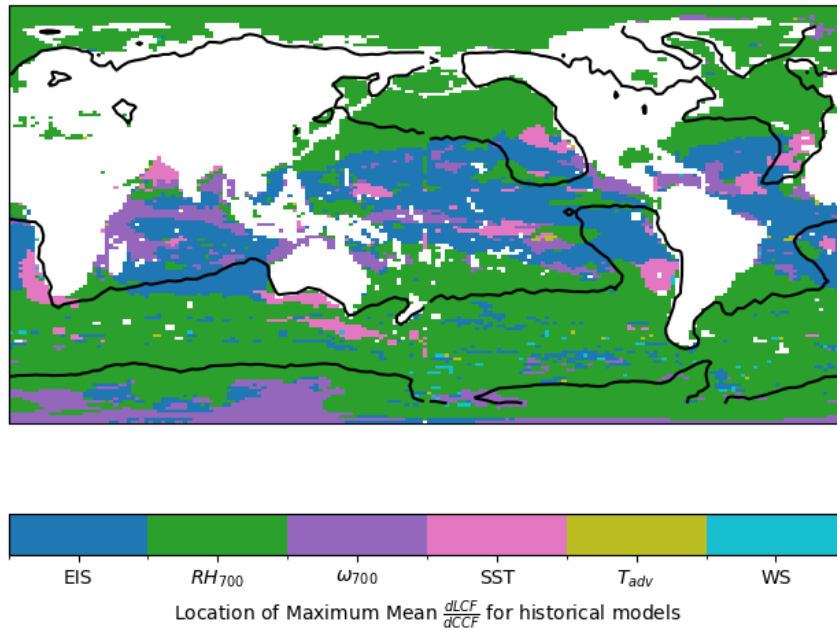


Figure 31: Maximum magnitude contributor to the multiple regression model of historical low cloudiness-meteorology relationships at each grid point.

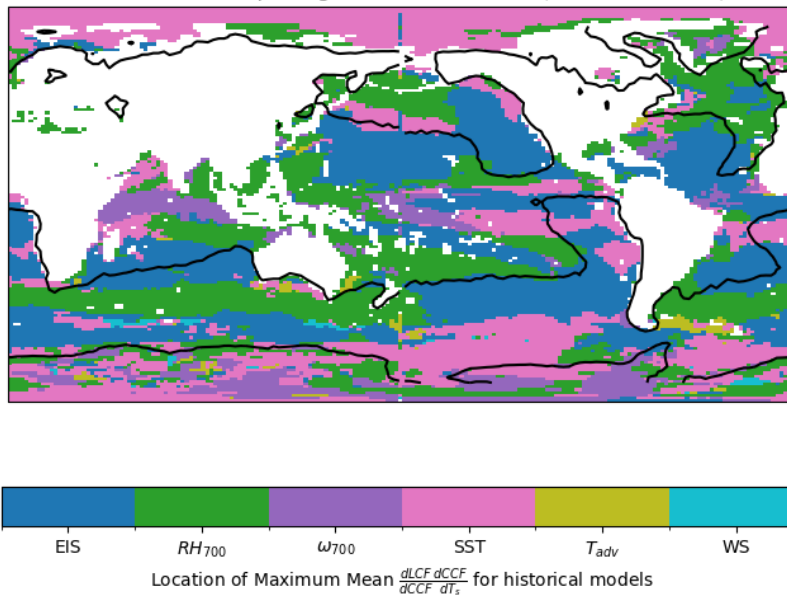


Figure 32: Maximum magnitude contributor of historical low cloudiness-global mean surface temperatures relationships through each CCF at each grid point.

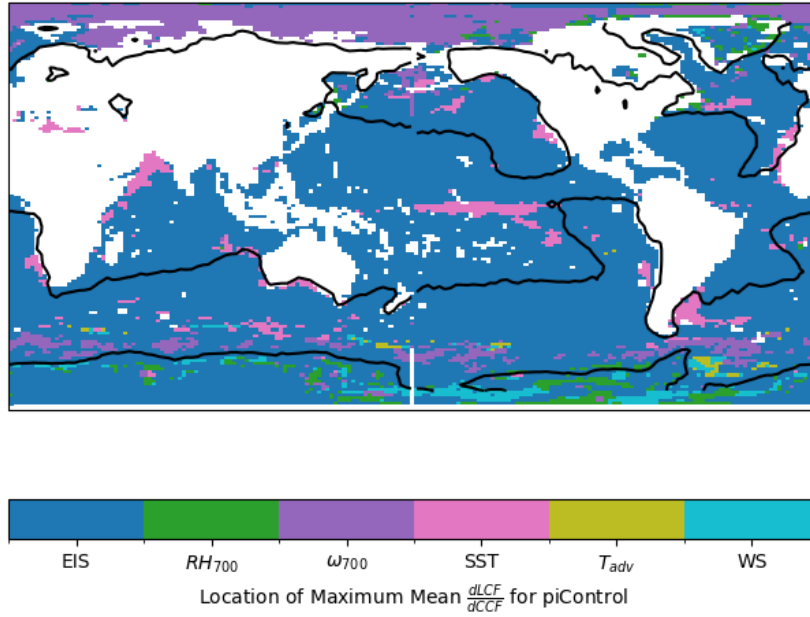


Figure 33: Maximum magnitude contributor to the multiple regression model of piControl low cloudiness-meteorology relationships at each grid point.

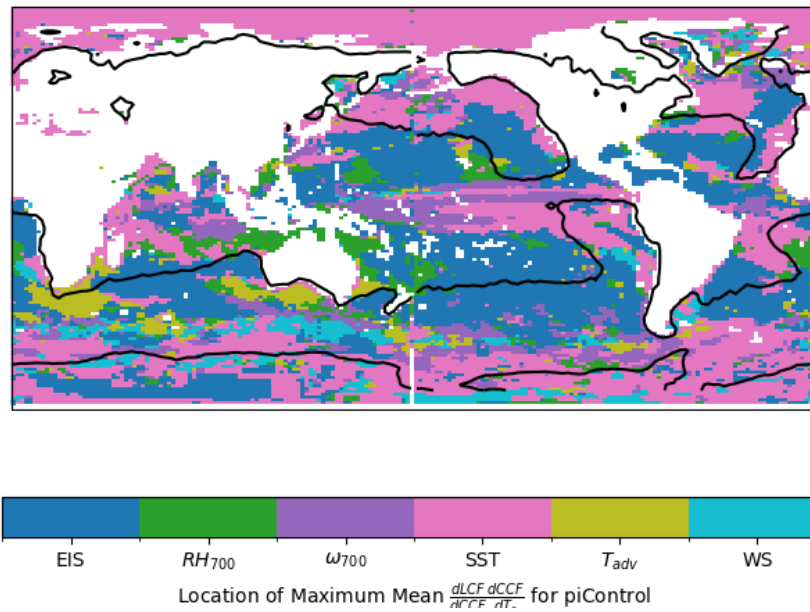


Figure 34: Maximum magnitude contributor of piControl low cloudiness-global mean surface temperatures relationships through each CCF at each grid point.

Comparison of directly regressed and reconstructed $\frac{DLCF}{DT_s}$ quantities across historical and piControl model ensembles.

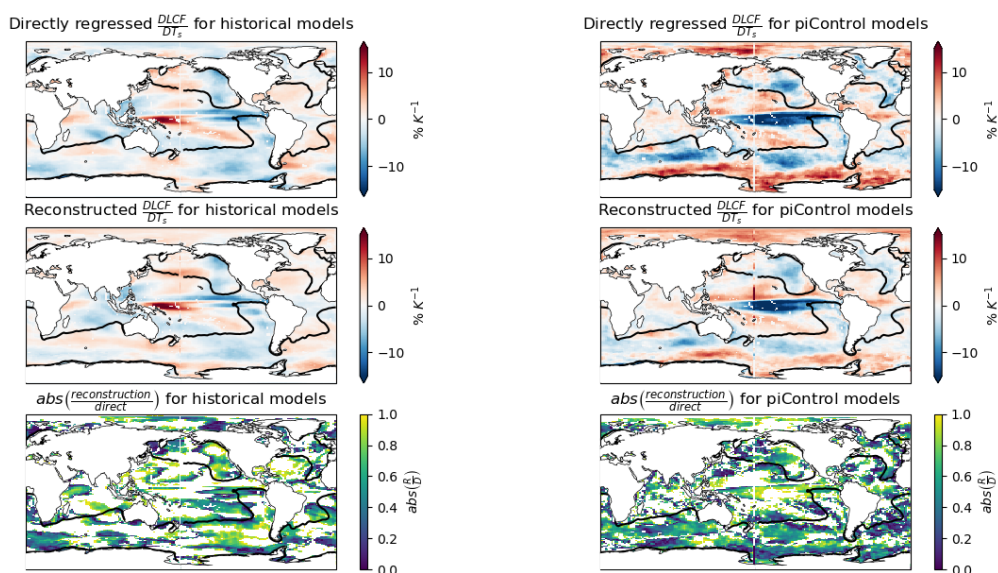


Figure 35: Comparison of directly regressed and reconstructed (as the sum of each term found in Figures 27 & 30) relationships between modeled low cloudiness and reanalyzed global mean surface temperature. Left to right, top to bottom: directly single-regressed historically modeled low cloudiness onto global mean surface temperatures; directly single-regressed piControl simulated low cloudiness onto global mean surface temperatures; reconstructed historically modeled Sc cloudiness and global mean surface temperature relationships; reconstructed piControl simulated low cloudiness and global mean surface temperature; ratio of reconstructed historical relationships to directly calculated relationships; ratio of reconstructed piControl relationships to directly calculated relationships.

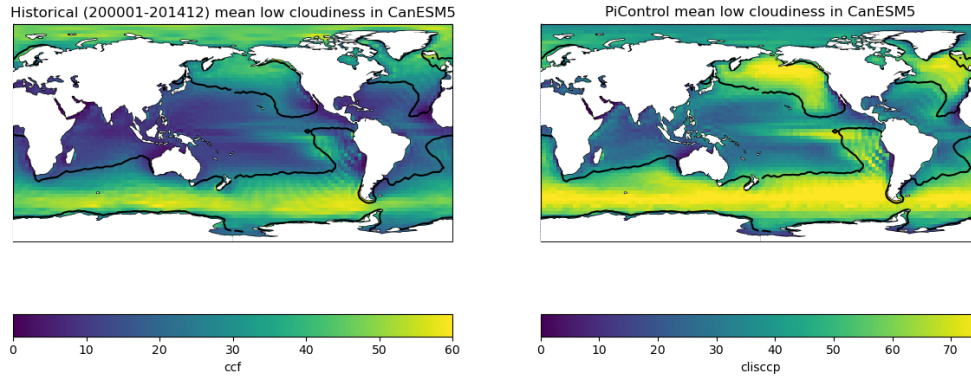


Figure 36: Comparison of cloudiness depiction from the same model across the two ensembles. Left: CanESM5 historically simulated low cloudiness; right: CanESM5 piControl ISCCP simulated low cloudiness.

V. References

- Bony, S., and J.-L. Dufresne, 2005: Marine boundary layer clouds at the heart of tropical cloud feedback uncertainties in climate models - Bony - 2005 - Geophysical Research Letters - Wiley Online Library.
<https://agupubs.onlinelibrary.wiley.com/doi/full/10.1029/2005GL023851> (Accessed October 11, 2023).
- , and Coauthors, 2015: Clouds, circulation and climate sensitivity. *Nature Geosci*, **8**, 261–268, <https://doi.org/10.1038/ngeo2398>.
- , and Coauthors, 2017: EUREC4A: A Field Campaign to Elucidate the Couplings Between Clouds, Convection and Circulation. *Surv Geophys*, **38**, 1529–1568, <https://doi.org/10.1007/s10712-017-9428-0>.
- Boucher, O., D. Randall, P. Artaxo, C. Bretherton, G. Feingold, P. Forster, V.-M. Kerminen, Y. Kondo, H. Liao, U. Lohmann, P. Rasch, S.K. Satheesh, S. Sherwood, B. Stevens and X.Y. Zhang, 2013: Clouds and Aerosols. In: Climate Change 2013: The Physical Science Basis. Contribution of Working Group I to the Fifth Assessment Report of the Intergovernmental Panel on Climate Change [Stocker, T.F., D. Qin, G.-K. Plattner, M. Tignor, S.K. Allen, J. Boschung, A. Nauels, Y. Xia, V. Bex and P.M. Midgley (eds.)]. Cambridge University Press, Cambridge, United Kingdom and New York, NY, USA.
- Bretherton, C. S., and P. N. Blossey, 2014: Low cloud reduction in a greenhouse-warmed climate: Results from Lagrangian LES of a subtropical marine cloudiness transition. *Journal of Advances in Modeling Earth Systems*, **6**, 91–114, <https://doi.org/10.1002/2013MS000250>.
- Ceppi, P., F. Briant, M. D. Zelinka, and D. L. Hartmann, 2017: Cloud feedback mechanisms and their representation in global climate models. *WIREs Climate Change*, **8**, e465, <https://doi.org/10.1002/wcc.465>.
- Cesana, G., A. D. Del Genio, and H. Chepfer, 2019: The Cumulus And Stratocumulus CloudSat-CALIPSO Dataset (CASCCAD). *Earth System Science Data*, **11**, 1745–1764, <https://doi.org/10.5194/essd-11-1745-2019>.
- Cesana, G. V., and A. D. Del Genio, 2021: Observational constraint on cloud feedbacks suggests moderate climate sensitivity. *Nat. Clim. Chang.*, **11**, 213–218, <https://doi.org/10.1038/s41558-020-00970-y>.
- Cesana, G. V., A. S. Ackerman, N. Črnivec, R. Pincus, and H. Chepfer, 2023: An observation-based method to assess tropical stratocumulus and shallow cumulus clouds and feedbacks in CMIP6 and CMIP5 models. *Environ. Res. Commun.*, **5**, 045001, <https://doi.org/10.1088/2515-7620/acc78a>.

- Eyring, V., S. Bony, G. A. Meehl, C. A. Senior, B. Stevens, R. J. Stouffer, and K. E. Taylor, 2016: Overview of the Coupled Model Intercomparison Project Phase 6 (CMIP6) experimental design and organization. *Geosci. Model Dev.*, **9**, 1937–1958, <https://doi.org/10.5194/gmd-9-1937-2016>.
- Gelaro, R., and Coauthors, 2017: The Modern-Era Retrospective Analysis for Research and Applications, Version 2 (MERRA-2). *Journal of Climate*, **30**, 5419–5454, <https://doi.org/10.1175/JCLI-D-16-0758.1>.
- Hersbach, H., and Coauthors, 2020: The ERA5 global reanalysis. *Quarterly Journal of the Royal Meteorological Society*, **146**, 1999–2049, <https://doi.org/10.1002/qj.3803>.
- Hill, P. G., C. E. Holloway, M. P. Byrne, F. H. Lambert, and M. J. Webb, 2023: Climate Models Underestimate Dynamic Cloud Feedbacks in the Tropics. *Geophysical Research Letters*, **50**, e2023GL104573, <https://doi.org/10.1029/2023GL104573>.
- Huang, B., C. Liu, V. Banzon, E. Freeman, G. Graham, B. Hankins, T. Smith, and H.-M. Zhang, 2021: Improvements of the Daily Optimum Interpolation Sea Surface Temperature (DOISST) Version 2.1, *Journal of Climate*, **34**, 2923–2939. doi: 10.1175/JCLI-D-20-0166.1
- IPCC 4th Assessment Glossary, AR4 WGI Annexes - Glossary A-D. *IPCC*, https://archive.ipcc.ch/publications_and_data/ar4/wg1/en/annexessglossary-a-d.html (Accessed October 11, 2023).
- Klein, S. A., and D. L. Hartmann, 1993: The Seasonal Cycle of Low Stratiform Clouds. *Journal of Climate*, **6**, 1587–1606, [https://doi.org/10.1175/1520-0442\(1993\)006<1587:TSCOLS>2.0.CO;2](https://doi.org/10.1175/1520-0442(1993)006<1587:TSCOLS>2.0.CO;2).
- , A. Hall, J. R. Norris, and R. Pincus, 2017: Low-Cloud Feedbacks from Cloud-Controlling Factors: A Review. *Surv Geophys*, **38**, 1307–1329, <https://doi.org/10.1007/s10712-017-9433-3>.
- Mieslinger, T., Á. Horváth, S. A. Buehler, and M. Sakradzija, 2019: The Dependence of Shallow Cumulus Macrophysical Properties on Large-Scale Meteorology as Observed in ASTER Imagery. *Journal of Geophysical Research: Atmospheres*, **124**, 11477–11505, <https://doi.org/10.1029/2019JD030768>.
- Myers, T. A., and J. R. Norris, 2016: Reducing the uncertainty in subtropical cloud feedback. *Geophysical Research Letters*, **43**, 2144–2148, <https://doi.org/10.1002/2015GL067416>.
- Qu, X., A. Hall, S. A. Klein, and A. M. DeAngelis, 2015: Positive tropical marine low-cloud cover feedback inferred from cloud-controlling factors. *Geophysical Research Letters*, **42**, 7767–7775, <https://doi.org/10.1002/2015GL065627>.

- Schiro, K. A., H. Su, Y. Wang, B. Langenbrunner, J. H. Jiang, and J. D. Neelin, 2019: Relationships Between Tropical Ascent and High Cloud Fraction Changes With Warming Revealed by Perturbation Physics Experiments in CAM5. *Geophysical Research Letters*, **46**, 10112–10121, <https://doi.org/10.1029/2019GL083026>.
- Schiro, K. A., H. Su, G. Elsaesser, and J. H. Jiang, 2020: Greater tropical ascent area reduction linked to higher equilibrium climate sensitivity in CMIP6. **2020**, A064-0018.
- Schiro, K. A., and Coauthors, 2022: Model spread in tropical low cloud feedback tied to overturning circulation response to warming. *Nat Commun*, **13**, 7119, <https://doi.org/10.1038/s41467-022-34787-4>.
- Scott, R. C., T. A. Myers, J. R. Norris, M. D. Zelinka, S. A. Klein, M. Sun, and D. R. Doelling, 2020: Observed Sensitivity of Low-Cloud Radiative Effects to Meteorological Perturbations over the Global Oceans. *Journal of Climate*, **33**, 7717–7734, <https://doi.org/10.1175/JCLI-D-19-1028.1>.
- Sherwood, S., S. Bony, and J.-L. Dufresne, 2014: Spread in model climate sensitivity traced to atmospheric convective mixing. *Nature*, **505**.
- Su, H., L. Wu, C. Zhai, J. H. Jiang, J. D. Neelin, and Y. L. Yung, 2020: Observed Tightening of Tropical Ascent in Recent Decades and Linkage to Regional Precipitation Changes. *Geophysical Research Letters*, **47**, e2019GL085809, <https://doi.org/10.1029/2019GL085809>.
- Tselioudis, G., W. B. Rossow, C. Jakob, J. Remillard, D. Tropf, and Y. Zhang, 2021: Evaluation of Clouds, Radiation, and Precipitation in CMIP6 Models Using Global Weather States Derived from ISCCP-H Cloud Property Data. *Journal of Climate*, **34**, 7311–7324, <https://doi.org/10.1175/JCLI-D-21-0076.1>.
- Vial, J., J.-L. Dufresne, and S. Bony, 2013: On the interpretation of inter-model spread in CMIP5 climate sensitivity estimates. *Clim Dyn*, **41**, 3339–3362, <https://doi.org/10.1007/s00382-013-1725-9>.
- Vogel, R., L. Nuijens, and B. Stevens, 2016: The role of precipitation and spatial organization in the response of trade-wind clouds to warming. *Journal of Advances in Modeling Earth Systems*, **8**, 843–862, <https://doi.org/10.1002/2015MS000568>.
- , A. L. Albright, J. Vial, G. George, B. Stevens, and S. Bony, 2022: Strong cloud–circulation coupling explains weak trade cumulus feedback. *Nature*, **612**, 696–700, <https://doi.org/10.1038/s41586-022-05364-y>.
- Webb, M. J., and Coauthors, 2006: On the contribution of local feedback mechanisms to the range of climate sensitivity in two GCM ensembles. *Clim Dyn*, **27**, 17–38, <https://doi.org/10.1007/s00382-006-0111-2>.

Wodzicki, K. R., and A. D. Rapp, 2022: More Intense, Organized Deep Convection With Shrinking Tropical Ascent Regions. *Geophysical Research Letters*, **49**, e2022GL098615, <https://doi.org/10.1029/2022GL098615>.

Yue, Q., B. H. Kahn, E. J. Fetzer, and J. Teixeira, 2011: Relationship between marine boundary layer clouds and lower tropospheric stability observed by AIRS, CloudSat, and CALIOP. *Journal of Geophysical Research: Atmospheres*, **116**, <https://doi.org/10.1029/2011JD016136>.